Monthly Notices of the ROYAL ASTRONOMICAL SOCIETY

MNRAS **536,** 1538–1554 (2025) https://doi.org/10.1093/mnras/stae2582
Advance Access publication 2024 November 19

NGTS-33b: a young super-Jupiter hosted by a fast-rotating massive hot star

Douglas R. Alves [1,2★] James S. Jenkins,[2,3★] Jose I. Vines,[4★] Matthew P. Battley,[5] Monika Lendl [5] François Bouchy,[5] Louise D. Nielsen [6] Samuel Gill,[7,8] Maximiliano Moyano,[4] D. R. Anderson,[4] Matthew R. Burleigh,[7] Sarah L. Casewell [7] Michael R. Goad,[7] Faith Hawthorn [7,8] Alicia Kendall,[9] James McCormac,[7,8] Ares Osborn,[10] Alexis M. S. Smith [11] Stéphane Udry,[5] Peter J. Wheatley [7,8] Suman Saha,[2,3] Léna Parc,[5] Arianna Nigioni,[5] Ioannis Apergis [7,8] and Gavin Ramsay [12]

[1]*Departamento de Astronomía, Universidad de Chile, Casilla 36-D, 7591245, Santiago, Chile*
[2]*Centro de Astrofísica y Tecnologías Afines (CATA), Casilla 36-D, 7591245, Santiago, Chile*
[3]*Instituto de Estudios Astrofísicos, Facultad de Ingeniería y Ciencias, Universidad Diego Portales, Av. Ejército 441, 8320000, Santiago, Chile*
[4]*Instituto de Astronomía, Universidad Católica del Norte, Angamos 0610, 1270709 Antofagasta, Chile*
[5]*Departement d'Astronomie, Université de Genève, 51 chemin Pegasi, CH-1290 Sauverny, Switzerland*
[6]*University Observatory, Faculty of Physics, Ludwig-Maximilians-Universität München, Scheinerstraße 1, D-81679 Munich, Germany*
[7]*Department of Physics, University of Warwick, Gibbet Hill Road, Coventry CV4 7AL, UK*
[8]*Centre for Exoplanets and Habitability, University of Warwick, Gibbet Hill Road, Coventry CV4 7AL, UK*
[9]*School of Physics and Astronomy, University of Leicester, Leicester LE1 7RH, UK*
[10]*Department of Physics and Astronomy, McMaster University, 1280 Main St W, Hamilton, ON, L8S 4L8, Canada*
[11]*Department of Extrasolar Planets and Atmospheres, Institute of Planetary Research, German Aerospace Center (DLR), Rutherfordstraße 2, D-12489 Berlin, Germany*
[12]*Armagh Observatory and Planetarium, College Hill, Armagh, BT61 9DG, UK*

Accepted 2024 November 13. Received 2024 November 8; in original form 2024 August 8

ABSTRACT

In the last few decades, planet search surveys have been focusing on solar-type stars, and only recently the high-mass regimes. This is mostly due to challenges arising from the lack of instrumental precision, and more importantly, the inherent active nature of fast-rotating massive stars. Here, we report NGTS-33b (TOI-6442b), a super-Jupiter planet with mass, radius, and orbital period of $3.6 \pm 0.3\,M_J$, $1.64 \pm 0.07\,R_J$, and $2.827\,972 \pm 0.000\,001$ d, respectively. The host is a fast-rotating (0.6654 ± 0.0006 d) and hot ($T_{\rm eff} = 7437 \pm 72$ K) A9V type star, with a mass and radius of $1.60 \pm 0.11\,M_\odot$ and $1.47 \pm 0.06\,R_\odot$, respectively. Planet structure and gyrochronology models show that NGTS-33 is also very young with age limits of 10–50 Myr. In addition, membership analysis points towards the star being part of the Vela OB2 association, which has an age of $\sim$ 20–35 Myr, thus providing further evidence about the young nature of NGTS-33. Its low bulk density of 0.19 ± 0.03 g cm^{-3} is 13 per cent smaller than expected when compared to transiting hot Jupiters (HJs) with similar masses. Such cannot be solely explained by its age, where an up to 15 per cent inflated atmosphere is expected from planet structure models. Finally, we found that its emission spectroscopy metric is similar to *JWST* community targets, making the planet an interesting target for atmospheric follow-up. Therefore, NGTS-33b's discovery will not only add to the scarce population of young, massive and HJs, but will also help place further strong constraints on current formation and evolution models for such planetary systems.

Key words: techniques: photometric – techniques: radial velocities – planets and satellites: detection – planets and satellites: general – stars: general.

1 INTRODUCTION

The detection of the first hot Jupiters (HJs; Mayor & Queloz 1995; Charbonneau et al. 2000) set a great milestone in the exoplanet field, paving the way to the detection of several more extrasolar planets. Ground-based spectroscopic (Valenti & Fischer 2005; Jenkins et al. 2009) and photometric surveys (Bakos et al. 2004; Pollacco et al. 2006; Wheatley et al. 2013) were initially responsible for the detection and characterization of several massive HJs. Yet, though challenging, a few Neptunes (e.g. HAT-P-11b, NGTS-14Ab; Bakos et al. 2010; Smith et al. 2021) have also been confirmed. Such selection bias towards massive planets is mostly due to the larger Doppler signal as well as transit depths induced by HJs given their mass and short orbital periods ($P < 10$ d), making their

★ E-mail: douglasalvesastro12@gmail.com (DRA); james.jenkins@mail.udp.cl (JSJ); jose.vines.1@gmail.com (JIV)

detection more favourable compared to less massive and/or longer period worlds. Besides that, ground-based missions are limited by atmospheric conditions (Cubillos et al. 2016; O'Brien et al. 2022) as well as the day–night cycle, hence challenging the discovery of long-period planets. On the other hand, space-based missions such as CoRoT (Auvergne et al. 2009), *Kepler*/K2 (Borucki et al. 2010), and the *Transiting Exoplanet Survey Satellite* (*TESS*; Ricker et al. 2015) were free of such atmospheric limitations, helping to reduce the bias by increasing the number of planet detections[1] significantly, with Kepler being responsible for the discovery of several (mini-)Neptunes ($10 \leq M < 38\,M_{\oplus}$) and (super-)Earths ($1 \leq M < 10\,M_{\oplus}$), whilst providing robust statistical constraints on planet occurrence rates (Mulders, Pascucci & Apai 2015; Hsu et al. 2019), as well as the multiplicity nature of rocky worlds (Cochran et al. 2011; Gillon et al. 2017). In addition, the dearth of Neptune planets with orbital periods interior to 4 d, known as the Neptune desert, first dropped out of the Kepler data, and subsequently corroborated by the relatively low Neptune discoveries from *TESS* mission. Though rare, planets have been detected and characterized in this region (e.g. LTT9779b; Jenkins et al. 2020; Hoyer et al. 2023; Fernández Fernández et al. 2024), which were fundamental to constrain the most likely scenario for these planets. In addition, the evolution of giant planets may even be associated to the emergence and form of the desert, where a combination of tidal migration with atmospheric photoevaporation (Lopez & Fortney 2013; Owen & Wu 2017) may have been able to strip off the migrating giants' envelopes, giving rise to a population of Neptune-desert planets.

Like the Neptune desert planets, the HJ population remains subjected to intense scrutiny, especially the transiting HJs (THJs), where besides their masses, radii (R_p) and bulk densities (ρ_p) can be estimated at high precision. Moreover, atmospheric follow-up may help reveal key properties (e.g, day–night temperatures, albedos/reflectivity and atmosphere abundances), making them great test beds for probing giant planet formation and evolution histories. For instance, HJs are not expected to form *in situ* but farther out in the disc where an initial $\sim 10\,M_{\oplus}$ protocore mass is fundamental to the onset of a runaway gas accretion process leading to the formation of giant planets (Pollack et al. 1996; Alibert et al. 2005; Piso & Youdin 2014). In addition, HJs formation and disc migration must occur quickly ($\sim$ 5–10 Myr), with time-scales being a function of the protostar mass as well as the disc properties, specially its mass and metallicity (see Fortney, Dawson & Komacek 2021). In fact, it has been noted that stellar metallicity ([Fe/H]) correlates with giant planet fraction (f_p), indicating that such planets are formed more effectively around metal-rich stars (Gonzalez 1997; Santos, Israelian & Mayor 2001; Fischer & Valenti 2005; Osborn & Bayliss 2020). Moreover, an increase in [Fe/H]leads to a higher f_p, providing further evidence that disc metallicity plays an important role in the formation of giant planets (Santerne et al. 2016; Buchhave et al. 2018; Barbato et al. 2019). For instance, Jenkins et al. (2017) find a correlation between giant hosts [Fe/H] and P, where the population of giants exterior to $P \leq 100$ d are more metal-rich with a [Fe/H] mean difference ~ 0.16 dex. Therefore, they point out that such correlation may indicate the initial location where giant planets formed in the protoplanetary disc. Finally, giant planets seem to be more abundant around more massive stars, where higher f_p are observed as a function of stellar mass (Johnson et al. 2010; Reffert et al. 2015; Jones et al. 2016). Such results point to a correlation between the central star and disc masses, where the former plays an important role in the type of planets that will be formed. In other words, an increase in the stellar mass leads to higher disc masses, hence more material with which to quickly form massive giant planets before the disc disperses. Therefore, these results are in agreement with the current findings of massive stars harbouring massive gas giant planets, particularly at short periods where the HJ population is located.

As mentioned, the evolution of giant planets may have been subjected to disc migration rather than *in situ* formation. Further evidence against the latter includes the detection of atmospheric escape in HJs (e.g. HD 209458b, HD 189733b, KELT-19b; Vidal-Madjar et al. 2003; Des Etangs et al. 2010; Wyttenbach et al. 2020) and high obliquities of close-in giants, which may be explained by the planets' evolution through high eccentricity (e) migration by secular interactions with outer companions (Fortney et al. 2021; Vick, Su & Lai 2023). In fact, a handful of hot hosts have massive HJs with non-zero obliquities (e.g. KELT-17b, MASCARA-1b, and TOI-1431b), with some even retrograde (HAT-P-14b; Winn et al. 2011), whereas cool stars tend to have HJs with low obliquities (Winn et al. 2011), thus showing that massive giant planets might have gone through multiple migration channels.

Here, we report the detection of NGTS-33b, the first Next Generation Transit Survey (NGTS) discovery of a super-Jupiter hosted by a massive star. This detection will add to the small, but growing number of massive systems, that will help us to better understand the formation and evolution processes of massive planets around hot stars. The manuscript is organized as follows, in Section 2, we present the photometry extraction from NGTS and *TESS* light curves, spectroscopic follow-up with FEROS, HARPS, and CORALIE and their respective spectral line activity diagnosis. Section 3 describes the data analysis, where we extract stellar parameters (Section 3.2), assess its age (Section 3.2.1), perform a global modelling to derive the planetary parameters (Section 3.3). Stellar rotation period, transit-timing variation (TTV) as well as dynamical stability were probed in Sections 3.1, 3.4, and 3.5, respectively. Finally, we discuss our results in Section 4 and set out the conclusions in Section 5.

1.1 The Next Generation Transit Survey

The NGTS (Chazelas et al. 2012; McCormac et al. 2017; Wheatley et al. 2018) is located at the ESO Paranal Observatory in Chile, with the objective of detecting new transiting planetary systems. The consortium has 12 telescopes with 0.2-m diameter each, and individual fields of view of 8 deg^2, which combined provides a wide-field of 96 deg^2.

The NGTS detectors host 2K×2K pixels, with individual pixels measuring 13.5 μm, which corresponds to an on-sky size of 5 arcsec pixel^{-1}, thus providing high-sensitivity images over a wavelength domain between 520 and 890 nm. This combination allows 150 ppm photometry to be obtained on bright stars ($V<10$ mag) for multicamera observations, while for single telescope mode at 30 min cadence, a precision of 400 ppm is achievable (Bayliss et al. 2022). The project has been operational since 2016 February, and over the past 8 yr has so far acquired over 400 billion measurements of over 30 million stars. Within this treasure-trove of data, the NGTS has discovered 26 new planetary systems (e.g. Bayliss et al. 2018; Bryant et al. 2020; Tilbrook et al. 2021; Bouchy et al. 2024), with more yet to be confirmed. A few of the highlights include the discovery of the Neptune desert planet NGTS-4b (West et al. 2019), an ultrashort period Jupiter NGTS-6b (Vines et al. 2019), the shortest period HJ NGTS-10b around a K5V star (McCormac et al. 2020), an inflated HJ around a low-mass and metal-poor K dwarf (Alves et al. 2022),

[1] 5675 planets on 2024 May 15 according to https://exoplanet.eu/.

Table 1. NGTS and *TESS* observation settings.

Start date	NGTS Mission End date	Nights	Camera
2019-Dec-18	2020-Mar-21	94	803
2020-Sep-28	2021-Mar-25	178	804
2021-Apr-26	2021-Jun-12	47	809
	TESS Mission		
Start date	End date	Sector	Camera
2019-Jan-07	2019-Feb-2	07	03
2020-Dec-17	2021-Jan-13	33	03
2021-Jan-13	2021-Feb-09	34	03
2023-Jan-18	2023-Feb-12	61	03

Table 2. NGTS and *TESS* photometry for NGTS-33.

Time ($BJD_{TDB}-2457000$)	Flux (normalized)	Flux error	Instrument
–	–	–	–
1491.65978	1.0004	0.0005	*TESS*
1491.68061	1.0003	0.0005	*TESS*
1491.70144	0.9995	0.0005	*TESS*
1491.72228	0.9991	0.0005	*TESS*
1491.74311	0.9991	0.0005	*TESS*
–	–	–	–
1836.59516	0.9964	0.0019	NGTS
1836.59658	1.0012	0.0032	NGTS
1836.59792	0.9944	0.0029	NGTS
1836.59933	0.9969	0.0014	NGTS
1836.60074	0.9972	0.0023	NGTS
–	–	–	–
2201.74242	0.9983	0.0009	*TESS*
2201.74936	0.9988	0.0009	*TESS*
2201.75631	0.9992	0.0009	*TESS*
2201.76325	1.0011	0.0009	*TESS*
2201.77020	1.0015	0.0009	*TESS*
–	–	–	–
2229.04839	0.9985	0.0009	*TESS*
2229.05534	0.9997	0.0009	*TESS*
2229.06228	1.0003	0.0000	*TESS*
2229.06923	1.0005	0.0009	*TESS*
–	–	–	–
2962.80386	0.9977	0.0006	*TESS*
2962.80849	1.0031	0.0018	*TESS*
2962.81544	0.9989	0.0008	*TESS*
2962.82238	0.9995	0.0025	*TESS*
2962.82933	1.0002	0.0012	*TESS*

Notes. The full Table is available in a machine-readable format from the online journal. A portion is shown here for guidance.

and a few warm planets (e.g. NGTS-29b, NGTS-30b; Battley et al. 2024; Gill et al. 2024).

2 OBSERVATIONS

Here, we describe the photometry and spectroscopic data acquisition and reduction that lead to the discovery of NGTS-33b . Tables 1, 2, and 3 show the NGTS and *TESS* observation dates and settings, a portion of the normalized photometry and radial–velocity (RV) used in the analysis, respectively.

Table 3. NGTS-33 follow-up RVs from FEROS, HARPS, and CORALIE.

BJD_{TDB} –2457000	RV ($m\,s^{-1}$)	RV err ($m\,s^{-1}$)	INSTRUMENT ($m\,s^{-1}$)
2852.87014602	19351.7	89.7	FEROS
2853.85667801	18666.5	94.2	FEROS
–	–	–	–
3317.55154657	18602.2	32.4	HARPS
3318.55134786	18553.0	36.6	HARPS
–	–	–	–
3396.64685773	18466.2	101.3	CORALIE
3398.57967810	19397.1	102.4	CORALIE

2.1 NGTS photometry

NGTS-33 observations were taken during 2019–2021 in single camera mode and with 10 s exposure time per frame, as summarized in Table 1. Three independent telescopes were used at different epochs, yielding a total of 309 426 images from which stellar brightness was measured by aperture photometry with the CASUTools[2] package. As part of the data reduction, an adapted version of the SysRem algorithm (Tamuz, Mazeh & Zucker 2005) and the box least-squares fitting algorithm (Kovács, Zucker & Mazeh 2002; Collier Cameron et al. 2006) `ORION` were used to remove nightly trends caused by atmospheric extinction and search for periodic transits in the timeseries, respectively. 28 transits in total were detected, from which seven had complete time coverage. A strong signal was detected at 2.83 d, and a validation process began in order to either confirm the signal as a THJ or reject it as a false positive detection. For example, one of the vetting tests deal with background eclipsing binaries, where consecutive transits showing odd–even and/or V-shaped morphologies could indicate candidates are false positives. NGTS-33 passed every validation step, and therefore further photometry and RV follow-up were obtained. Fig. 1 shows the NGTS detection light curve wrapped around the best-fitting period $2.827\,969 \pm 0.000\,002$ d computed from the global modelling (Section 3.3). For a thorough description of the NGTS mission, data reduction, and acquisition, we refer the reader to Wheatley et al. (2018).

2.2 *TESS* photometry

TESS (Ricker et al. 2015) observed NGTS-33 in Sectors 07, 33, 34, and 61 with cadences of 30, 5, 5, and 3.33 min, respectively. The data were acquired from the *Mikulski Archive for Space Telescopes*, using the `lightkurve` package (Lightkurve Collaboration et al. 2018). The first three sectors were available through distinct data reduction teams, to name a few, the Science Processing Operations Center (*TESS*–SPOC; Jenkins et al. 2016; Caldwell et al. 2020), the Quick Look Pipeline (QLP; Kunimoto et al. 2021), and the Cluster Difference Imaging Photometric Survey (CDIPS; Bouma et al. 2019), with the latter providing further evidence on the young nature of NGTS-33 (see Section 3.2.1). Sector 61 is thus far only available through the QLP pipeline, thus upon analysis of the data we opted to use *TESS*-SPOC light curves for Sectors 07, 33, and 34 as the data showed slightly less out of transit dispersion. Fig. 2 shows the detrended phase-folded light curve as well as the best-fitting transit model derived in Section 3.3.

[2]http://casu.ast.cam.ac.uk/surveys-projects/software-release

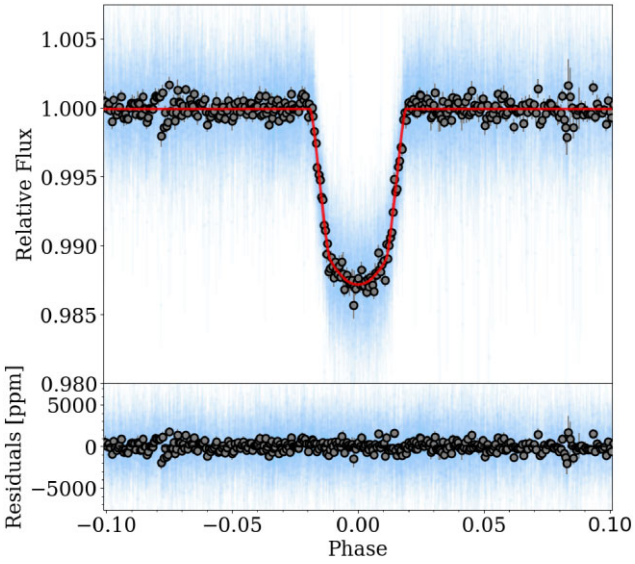

Figure 1. Top panel: NGTS detrended light curve phase-folded to the best-fitting period listed in Table 5 and zoomed to show the transit event. Blue and black circles correspond to modelled photometric data and binned data with the associated photon noise error. The red line and shaded region show the median transit model and its 1σ confidence interval. Bottom panel: residuals to the best-fitting model.

Lastly, we point out that the planet was independently detected by NGTS, despite *TESS* first observed the star in January 2019 with the release of Sector 07. The 30-min cadence photometry did not provide sufficient evidence for a planet candidate at that time, with a TOI alert issued nearly 4 yr later, on 2023 May 3, by which point NGTS had already gathered evidence for a confirmed planet. NGTS monitoring spanned from 2019 March to 2021 June, during which multiple transit events were detected prior to the release of *TESS* Sector 33 in 2020 December. Finally, our RV follow-up began on 2022 April 14, and continued until 2024 April 12, with NGTS-33b being labelled as TOI-6442 during this period.

2.3 Spectroscopic follow up

2.3.1 FEROS

19 high-resolution echelle spectra were obtained for NGTS-33 during UT 2022-04-14 through 2023-01-16 under the FEROS program ID 0110.A-9035(A) (PI: JIV) on the MPG/ESO 2.2-m (Kaufer et al. 1999) telescope at the La Silla Observatory in Chile. The 500–1200 s exposure times spectra were reduced using the automated CERES pipeline (Brahm, Jordán & Espinoza 2017), which performs all the steps in the cross-correlation function (CCF) reduction, optimally extracts the spectra and performs wavelength calibration, corrects for instrumental drift, and normalizes the continuum. CERES computes RVs using the CCF method using a G2 mask. Additionally, we obtain the bisector velocity spans (BIS) which track stellar activity, with any correlation between the BIS and the RVs providing evidence for instrumental, and/or stellar effects impacting the observed spectra. Finally, upon inspection of the reduced data, we dropped the first 4 RVs given their low signal-to-noise ratios (SNRs) and performed the global model in Section 3.3 with 15 FEROS RVs. Fig. 3 shows the phase-folded FEROS, HARPS and CORALIE RVs as well as the best-fitting K model derived in Section 3.3.

2.3.2 HARPS

We obtained 10 high-resolution echelle spectra for NGTS-33 during UT 2024-01-06 through 2024-01-10 under the HARPS program ID 112.25QD (PI: DRA) on the ESO 3.6 m (Mayor et al. 2003) telescope at the La Silla Observatory in Chile. The high accuracy mode (HAM) was used, where we achieved a typical SNR of 35 per pixel at 6500 Å and an RV precision of $\sim 37\,\mathrm{m\,s^{-1}}$ with exposure times of 1800-2100 s depending on weather and seeing conditions. The RV measurements were computed with the standard HARPS pipeline (Lovis & Pepe 2007) using the following binary masks for the cross-correlation: G2, K5, K0, and M4, where agreement was found amongst the RVs estimated with these binary masks. Given that NGTS-33 is an F-type star, we adopted the RVs measured from the cross-correlation with a G2 binary mask as it is the closest in spectral type to our target.

2.3.3 CORALIE

The Swiss 1.2 m (Queloz et al. 2000) at the La Silla observatory has been used to collect 11 high-resolution spectra with the CORALIE spectrograph. It has two fibres, with one centred on the target while the other directed to either the sky or the Fabry–Pérot (FP) etalon for purposes of background subtraction or simultaneous drift calibration, respectively. Our observations made use of the FP mode, where a spectral resolution of $\sim 60\,000$ and wavelength coverage of 390–680 nm allowed us to achieve a typical RV precision of $\sim 100\,\mathrm{m\,s^{-1}}$ during the data acquisition on 2024 February 27 through 2024 April 12 with 30-min exposure times. The spectra were reduced by the standard CORALIE pipeline, and RVs determined through the cross-correlation method with a binary G2 mask (Pepe et al. 2002). Further line diagnosis (e.g. FWHM–CCF and BIS) were also extracted during the data reduction.

2.3.4 Spectral diagnosis

RVs rely on the accurate measurement of spectral lines centroids. However, stellar activity could affect spectral line profiles, producing spurious periodic RV patterns that could mimic a planetary signal. Diagnosis of spectral lines is a common approach that provides further confidence on the planetary nature of the signal, where correlation between the RVs with parameters such as activity indexes, line bisectors (BIS) or their full width at half-maxima (FWHM) are a proxy for activity-induced RV variation, rather than a planetary nature. Therefore, we estimate the correlation between RVs against BIS and FWHM–CCF with the Pearson coefficient in equation (1),

$$r = \frac{\sum(RV_i - \bar{RV})(x_i - \bar{x})}{\sqrt{\sum(RV_i - \bar{RV})^2 \sum(x - x_i)^2}}, \quad (1)$$

where x_i and $\bar{x}$ represents the individual data points and their mean value for either BIS or FHWM. The r coefficient between the RVs and BIS for FEROS, HARPS, and CORALIE are 0.193, 0.081, and 0.32, respectively, while for the FWHM–CCF for FEROS, HARPS, and CORALIE, the r values are 0.02, 0.04, and –0.26, respectively. The Pearson r coefficient limits are –1 to 1, with values close to zero indicating that little correlation is present in the data sets. Finally, Fig. 4 shows the LS periodogram for BIS and FWHM computed from FEROS, HARPS, and CORALIE data, an offset was applied for better visualization. The false alarm probability (FAP) at the respective instrument highest periodogram peaks are marked as horizontal dashed lines, with no significant peak present at the orbital period of NGTS-33b.

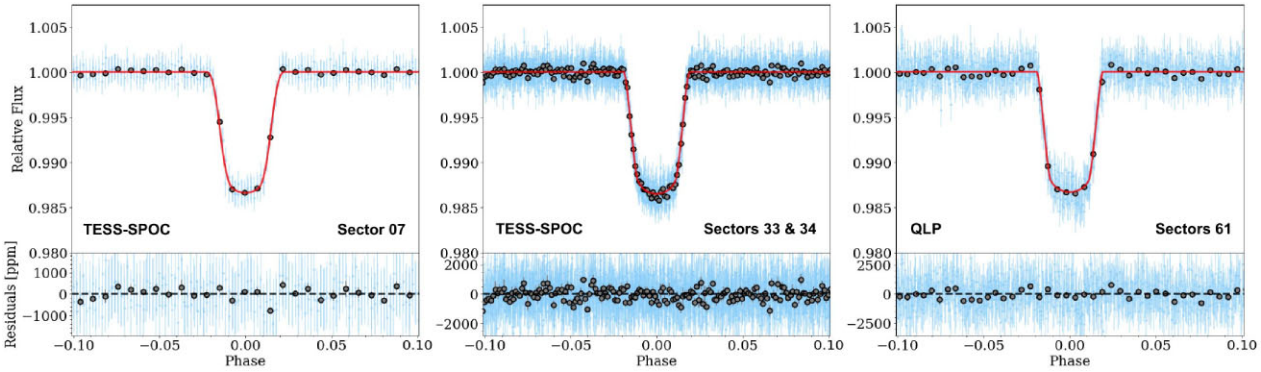

Figure 2. Left panel: phase-folded, 30-min detrended light curve from *TESS*-SPOC, Sector 07. Centre panel**:** the same as the left plot but for Sectors 34 and 35 at 5-min cadences. Right panel**:** phase-folded, 3.33-min detrended light curve from QLP, Sector 61. Colours and labels correspond to Fig. 1.

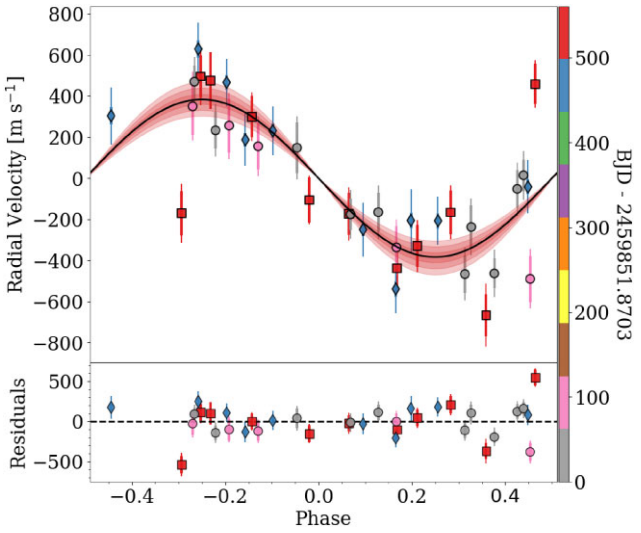

Figure 3. Top panel: RV phase-folded to the best-fitting period listed in Table 5. RV data are colour-coded in time with the black line and light red-shaded region showing the median transit model and its 1σ, 2σ, and 3σ confidence intervals. FEROS, HARPS, and CORALIE RVs are highlighted by the circles, diamonds and squares, respectively. Bottom panel: residuals to the best-fitting model.

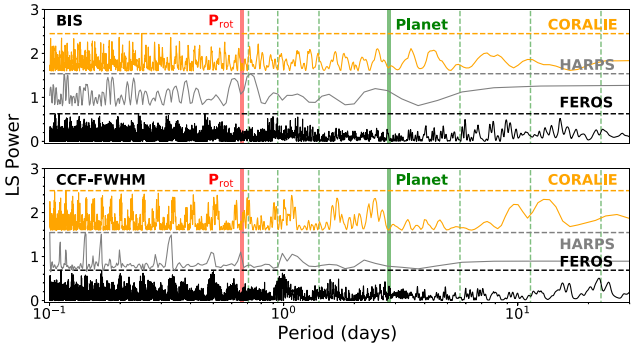

Figure 4. Periodogram of the line bisectors (top panel) and CCF–FWHM (bottom panel) for FEROS (in black), HARPS (in grey) and CORALIE (in yellow). The FAP level at the highest peak is shown as horizontal black, grey, and yellow lines for FEROS, HARPS, and CORALIE, respectively. The BIS and CCF-FWHM FAPs at highest peaks for FEROS, HARPS, and CORALIE are 0.06, 0.59, 0.05 and 0.04, 0.01, 0.02, respectively. The planet's orbital period is highlighted by the green vertical line with dashed lines showing the alias 1/8, 1/4, 1/2, 2, 3, and 4 from left to right, respectively, and the stellar rotation marked by the red vertical line.

Lastly, the *Gaia* DR3 catalogue was examined around NGTS-33 to exclude potential contamination from a background eclipsing binary. This search identified five neighbouring stars within the 21-arcsec *TESS* pixel, each with G magnitudes between 6.4 and 9.2 fainter than NGTS-33, and renormalized unit weight error values below 1.3. Although high-spatial-resolution imaging is unavailable, the NGTS pixel scale is four times finer than *TESS*, meaning that only one of these stars falls within the NGTS pixel. This star, named *GAIA* DR3 5590415817155700480, lies 3.1 arcsec from NGTS-33 and has a *G*-band magnitude of 20, thus contributing negligible flux in the aperture. Its distance also places it outside the 1 arcsec HARPS fibre. Additionally, the HARPS CCFs were inspected and show no evidence of wings or secondary dips typically seen in spectroscopic binaries, thus given our data set, it is unlikely that NGTS-33 is part of a binary systems.

3 DATA ANALYSIS

3.1 Stellar rotation analysis

The star's magnetic fields can prevent local convective motion in the photosphere, consequently blocking the radial heat transfer, thus leading to the appearance of darker and cooler spots compared to the surroundings. Such regions are associated to stellar spots, and are known to be more frequent with increasing stellar activity. As the star spins, its motion brings these spots in and out of sight, causing a periodic brightness variability in the photometric time-series. Therefore, the measurement of the stellar rotation is possible assuming the spot motions are solely due to the stellar spin.

Following the procedures laid out in previous NGTS rotation works (Gillen et al. 2020; Smith et al. 2023), we derived NGTS-33 rotation period with the Lomb–Scargle (LS; VanderPlas 2018) and the autocorrelation function (ACF; Kreutzer et al. 2023) methods. Both methods rely on distinct assumptions, thus having advantages and limitations. The LS method assumes a sinusoidal function to model the rotation signal, mostly suited for stars that present steady photometric variability, with spot time-scales larger than the rotation period. On the other hand, the ACF technique is a more flexible and model-free technique, which measures the degree of similarity between different parts of the data set (see McQuillan, Mazeh & Aigrain 2014; Gillen et al. 2020). To derive the best-fitting period from the ACF, we used the undamped simple harmonic oscillator described in Equation (2), with τ defining the decay time-scale, A

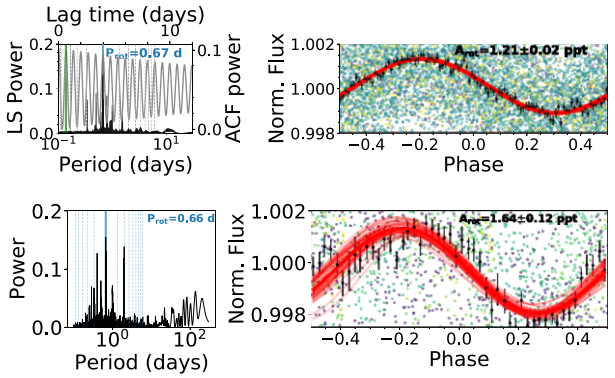

Figure 5. Top panel**:** the left panel shows the SPOC–*TESS* LS periodogram in black and ACF in grey, with the bottom and left axes representing the LS periodogram, while the top and left axes are for the ACF model. The vertical blue and green bars corresponding to the optimal periods from LS and ACF, respectively. The blue-coloured $P_{\rm rot}$ at the top right shows both the period at maximum power of the LS periodogram and the period from the ACF. The right panel shows the *TESS* data folded to the LS best-fitting period colour-coded by time evolving from yellow to purple. Black points are binned in phase domain, with a sinusoidal model and 50 realizations drawn from the final distribution shown in red. $A_{\rm rot}$ shows the median and 1σ best-fitting model. Bottom panel: the same as described in the top panel for NGTS data. The ACF is not shown as it did not converged likely due to the gaps in the NGTS data.

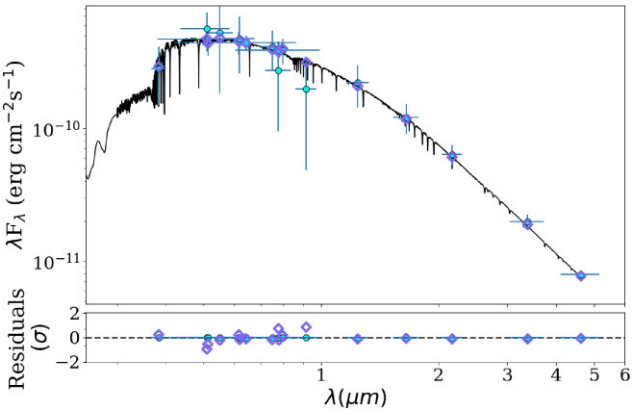

Figure 6. Top panel: the best-fitting spectral energy distribution model (black line) based on BT-Settl models given the NGTS-33 photometric data (cyan points) and their respective bandwidths are shown as horizontal error bars. Purple diamonds represent the synthetic magnitudes centred at the wavelengths of the photometric data from Table 4. Bottom panel: residuals to the best fit in σ units.

and B to adjust for the ACF power, and y_0 to adjust for the offset.

$$y(t) = \mathrm{e}^{\frac{-t}{\tau}}\left(A\cos\frac{2\pi t}{P_{\rm rot}} + B\cos\frac{4\pi t}{P_{\rm rot}}\right) + y_0. \quad (2)$$

Prior to the period search, we masked the transits, binned the data to 30-min cadences and median normalized it. Fig. 5 shows the LS periodogram and the ACF model in the top panel left. The green and blue vertical bars show that both methods agree to the same 0.67d periodic signal. The top right panel shows the folded light curve to the LS period at maximum power. We estimated a $P_{\rm rot}^{\rm TESS} = 0.6654 \pm 0.0006$ and $A_{\rm rot}^{\rm TESS} = 1.21 \pm 0.02$ ppt from LS periodograms with uncertainties from bootstraping with 10 000 iterations. For the NGTS photometry, the LS periodogram showed the 1 d peak as the main signal, which is commonly associated with the day–night cycles in ground-based missions. Upon removing it by applying a Savitzky–Golay filter, we did the same procedures described above to probe for rotation signatures. Fig. 5, in the left panel, shows the cleaned NGTS data periodogram, where the rotation peak of 0.66 d is present, and followed by its thi$^{\rm rd}$ harmonic marked in vertical-dashed lines. The rotation period and amplitude estimated from NGTS photometry is $P_{\rm rot}^{\rm NGTS} = 0.665 \pm 0.001$ and $A_{\rm rot}^{\rm NGTS} = 1.66 \pm 0.08$ ppt, with uncertainties estimated from bootstraping with 10 000 iterations. The ACF applied to NGTS did not converge due to the several gaps inherent in ground-based missions. The rotation periods from both instruments are in statistical agreement, while the NGTS amplitude is $\sim 6\sigma$ away from that measured by *TESS*. Such amplitude mismatch between *TESS* and NGTS is likely due to spot evolution between measurements from NGTS and *TESS*, though the instruments distinct photometric band-passes might have also played a role as spots contrast vary with wavelengths or a combination of both.

As *TESS* data are comprised of three distinct sectors, we repeated the analysis above on a per-sector basis. Although we recover the same 0.67 d signal, a second signal at $\sim$ 0.8 d is present and dominant in Sector 7, yet with an LS power difference of $\sim$ 1 per cent. Yet, for Sectors 33 and 34, the 0.67 d signal becomes more significant with a power difference of $\sim$ 7 and $\sim$ 10 per cent, respectively, thus why the rotation from the joint light curve favoured the 0.67 d period. In addition, the periods derived from ACF for Sectors 7, 33, and 34 are 0.8, 0.66, and 0.67 d, respectively, thus confirming the LS peaks. We have also carried out the same analysis for QLP light curves, and reached the same periods preferences from LS and ACF methods, thus implying that the results are pipeline independent and likely astrophysical. The LS periodogram on the QLP Sector 61 showed the 0.8 and 0.67 d periods at similar power, whereas the ACF period was 0.66 d. The NGTS periodogram shows the 0.67 d peak and its harmonics at a much larger power (Fig. 5, bottom panel) compared to the 0.8 d, which after subtracting the 0.67 d, it becomes apparent, with a measured $A_{\rm rot}$ of 0.90 ± 0.11, and power difference between the periods of $\sim$ 13 per cent, thus weaker than the main 0.67d signal. Although both 0.67 and 0.8 d signals are significant in the per-sector *TESS* analysis, we adopted the 0.67 d as it is (1) the dominant signal from the analysis in the joint light curve from both LS and ACF methods, (2) it is also the dominant peak in the NGTS data, and (3) its larger amplitude signal compared to the 0.8 d amplitude in *TESS* (0.63 ± 0.03 ppt) and NGTS (0.90 ± 0.11 ppt). None the less, the 0.67 and 0.8 d signals are likely astrophysical as they are present in both instruments. It is possible that due to the nature of fast rotators, spots could have been propelled towards higher latitudes through the coriolis force. As spots typical lifetimes are of a few days to months, it may be possible that *TESS* captured distinct spot distributions over Sector 7 where the 0.8 d dominates, and the two consecutive Sectors 33 and 34, with dominance on the 0.67 d signal. In order to rule out that any of the signals has its origin on UCAC4 271-014742, we repeat the rotation analysis for this star using the uncontaminated NGTS photometric time-series. We confirm the rotation period of $\sim$ 0.11 d from *Gaia*, and derive an amplitude of $A = 7.26 \pm 0.26$ ppt as shown in Fig. A3. As the 0.67 and 0.8 d are not present in the LS periodogram, with the ACF method is agreement with the LS period at maximum power, we conclude that both 0.67 and 0.8 d signals are likely originated from NGTS-33 rather than UCAC4 271-014742.

We investigated the possibility that the light-curve periodicity are related to pulsations rather than rotation. NGTS-33 stellar properties place it just outside the bottom of the instability strip

near the class of γ Doradus. Such stars are late A to early F spectral types, with masses between 1.4 and 2.0 $M_\odot$ and multiperiodic g mode induced variability with amplitudes no larger than 0.1 mag and periods of the order of 1 d. Although we do not completely rule out the pulsating nature of these signals, spot-crossing events observed in *TESS* provide robust evidence for the rotation nature of the photometric periodicity. Fig. A2 shows these events, with the first two transits from top to bottom displaying features consistent with spot-crossing, while the last transit, we interpret as a spot entering the line of sight, thus reducing the flux. Moreover, spot evolution could well explain the power variability of the 0.67 and 0.8 d signals due to distinct spot distributions as a function time. Additionally, line blending due to rotational broadening evidenced by the lack of Li as well as Fe lines to trace the host age and the projected velocity ($v\sin i_*$), respectively, provides further evidence that the photometric variability is indeed from a spot modulated time-series. Finally, an estimated value of $v\sin i_* \sim 111.87$ km s^{-1} was computed from the star's radius and adopted rotation period from Table 4. A measurement of $v\sin i_*$ was not possible due to a combination of low SNR, for example, HARPS SNR 28-35, and line blending. However, even though spectral lines are affected by several physical mechanisms (e.g. collisional broadening) depending on wavelength and stellar properties (e.g. $\log g$, $T_{\rm eff}$), the CCF shape provides a rough estimate of the averaged spectral line profile, from which we computed the HARPS FHWM–CCF to be $\sim$ 35–38 km s^{-1}. Rewriting the $v\sin i_*$ relation as $i_* = \arcsin \frac{v \sin i_*}{2\times\pi R_s/P_{\rm rot}}$ (see e.g. Hirano et al. 2014), and using the FHWM–CCF as proxy for $v\sin i_*$, we computed i_* to be about 18°–20°. This inclination is in agreement to (Dong & Foreman-Mackey 2023), which found that 72 ± 9 per cent of the systems with measured sky-projected stellar obliquities have values less than 40°. We point out that a more complete obliquity analysis will be presented in a follow-up paper where the Rossiter–McLaughlin for NGTS-33 will be investigated.

3.2 Stellar properties

NGTS-33 parameters were estimated using the publicly available*ARIADNEPYTHON* package (Vines & Jenkins 2022). The code is based on the spectral energy distribution (SED) fitting method, which consists of fitting archival photometry to synthetic magnitudes from interpolated grids of stellar atmosphere models. The synthetic photometry is computed from convolving a given model with several filter response functions (see available SED models in Vines & Jenkins 2022) and scaled by $(R_s/D)^2$, with D being the star's distance to the sun. An excess noise term is introduced for each photometric measurement in order to account for underestimated uncertainties. Finally, a cost function with input parameters $T_{\rm eff}$, $\log g$, [Fe/H], and V-band extinction (A_V) are minimized with DYNESTY (Speagle 2020), a nested sampling algorithm used to effectively search the parameter space, and find the best set of synthetic fluxes from a given SED model with stellar properties that best matches the observed photometry.

ariadne performs the above steps for several atmosphere libraries, to name a few, Phoenix V2 (Husser et al. 2013), BT-Settl (Hauschildt, Allard & Baron 1999; Allard, Homeier & Freytag 2012), Castelli & Kurucz (2004), and KURUCZ (1993). The code will output stellar posterior distributions from fits using each library, where the adopted stellar parameters are derived from the averaged posterior distributions weighted by their respective Bayesian evidences. Such a Bayesian averaging method helps to mitigate the assumptions and limitations from individual stellar atmosphere model, thus yielding precise stellar parameters, particularly the R_s and $T_{\rm eff}$, which are key to inform the global modelling of NGTS-33b (see Section 3.3). Finally, $T_{\rm eff}$, $\log g$, [Fe/H] as well as additional quantities such as D, R_s, and A_V from ARIADNE are used to automatically derive the stellar age (t_s), M_s, and the equal evolutionary points from the ISOCHRONE package (Morton 2015).

We set up ARIADNE with priors defined in Table A1, where $\mathcal{N}(\mu, \sigma^2)$ and $\mathcal{U}$(a, b) define normal and uniform priors with μ, σ^2, a, and b representing the median, variance, and lower and upper limits, respectively. We opted for priors somewhat centred around NGTS-33 *GAIA* DR3[3] parameters as preliminary tests with broad and uninformative priors were consistent with the values reported by *GAIA*, which are $T_{\rm eff} = 7213 \pm 9$ K, $\log g = 4.19^{+0.03}_{-0.01}$ dex, $R_s = 1.54^{+0.06}_{-0.03}$ $R_\odot$ distance of 447^{+17}_{-7} pc, $A_V = 0.334^{+0.004}_{-0.001}$, and

Table 4. Stellar properties for NGTS-33.

Property	Value	Source
Astrometric properties		
RA	$07^{\rm h}11^{\rm m}20\overset{\rm s}{.}0004$	*GAIA*
Dec.	$-35°51'1\overset{''}{.}8648$	*GAIA*
2MASS ID	J07112000 3551019	2MASS
TIC ID	97921547	TIC
GAIA DR3 ID	5590415817155428224	*GAIA*
Parallax (mas)	2.262 ± 0.012	*GAIA*
$\mu_{\rm RA}$ (mas y^{-1})	-4.936 ± 0.013	*GAIA*
$\mu_{\rm Dec.}$ (mas y^{-1})	6.538 ± 0.014	*GAIA*
Photometric properties		
V (mag)	11.458 ± 0.021	APASS
B (mag)	11.89 ± 0.028	APASS
g (mag)	11.655± 0.014	APASS
r (mag)	11.425 ± 0.012	APASS
i (mag)	11.385 ± 0.011	APASS
G (mag)	11.394 ± 0.003	*GAIA*
TESS (mag)	11.101 ± 0.006	TIC
J (mag)	10.607 ± 0.023	2MASS
H (mag)	10.475 ± 0.024	2MASS
K (mag)	10.408 ± 0.021	2MASS
W1 (mag)	10.366 ± 0.023	*WISE*
W2 (mag)	10.381 ± 0.019	*WISE*
W3 (mag)	10.508 ± 0.067	*WISE*
Derived properties		
ρ_* (g cm^{-3})	0.81± 0.02	EMPEROR
$\gamma_{\rm RV-HARPS}$ (km s^{-1})	$18.93^{+0.01}_{-0.07}$	EMPEROR
$\gamma_{\rm RV-CORALIE}$ (km s^{-1})	$18.72^{+0.02}_{-0.2}$	EMPEROR
$\gamma_{\rm RV-FEROS}$ (km s^{-1})	$18.90^{+0.07}_{-0.01}$	EMPEROR
$\sigma_{\rm HARPS}$ (m s^{-1})	141^{+59}_{-13}	EMPEROR
$\sigma_{\rm FEROS}$ (m s^{-1})	$90 \pm ^{+39}_{-29}$	EMPEROR
$\sigma_{\rm CORALIE}$ (m s^{-1})	$299 \pm ^{+86}_{-37}$	EMPEROR
$P_{\rm rot}$ (d)	0.6654 ± 0.0006	This work
$T_{\rm eff}$ (K)	7437 ± 72	ARIADNE
(Fe/H)	–0.11 ± 0.17	ARIADNE
log g	4.26± 0.28	ARIADNE
Age (Myr)	10–50	This work
M_s($M_\odot$)	1.60± 0.11	ARIADNE
R_s($R_\odot$)	1.47± 0.06	ARIADNE
Luminosity ($L_\odot$)	5.91 ± 0.54	ARIADNE
Distance (pc)	438.5 ± 7.1	ARIADNE

2MASS (Skrutskie et al. 2006); TIC v8 (Stassun et al. 2018); APASS (Henden et al. 2015); *WISE* (Wright et al. 2010); *Gaia* (Brown et al. 2021)

[3]https://gea.esac.esa.int/archive/

$t_s = 0.38^{+0.28}_{-0.18}$ Gyr. We point that the age is computed from the *GAIA* apsis FLAME module, which is obtained by comparing NGTS-33 the $T_{\rm eff}$ and luminosity with the BASTI (Hidalgo et al. 2018) solar metallicity stellar evolution models. ARIADNE computed stellar parameters are $T_{\rm eff} = 7437 \pm 72$, log g = 4.26 ± 0.28 dex, $R_s = 1.47 \pm 0.06$ $R_\odot$ $M_s = 1.60 \pm 0.11$ $M_\odot$ $\rho_* = 0.71 \pm 0.12$ g cm^{-3}, distance of 448.4 ± 7.3 pc, $A_V = 0.53 \pm 0.11$, and $t_s = 0.14 \pm 0.12$ Gyr. Fig. 6 shows the BT-Settl best-fitting SED model to the archival photometry with adopted median and 1σ posteriors distributions for the NGTS-33 stellar parameters shown in Table 4.

We have also attempted to measure NGTS-33 atmospheric properties ($T_{\rm eff}$, [Fe/H], log g, and sin i$_*$) from co-added HARPS spectra using SPECIES[4] (Soto & Jenkins 2018), a code that estimates atmospheric parameters from high-resolution spectra. However, the code could not converge due to a combination of factors, including limited spectral features, unresolved spectral lines for abundance measurement via equivalent widths, and a low SNR ratio (HARPS–SNR ∼ 40), partly due to its faint $V \sim 11.5$ mag. As a result, we opted for the SED-fitting method instead.

3.2.1 *Age estimation*

A typical method to estimate stellar ages consists of isochrone constructions through the usage of grids of pre-computed stellar evolutionary models described by stellar physical properties (e.g. $T_{\rm eff}$, L_*, [Fe/H], so forth) that are interpolated to fit a set of observed stellar parameters. Such evolutionary models are rearranged to tracks of fixed ages, named isochrones, from which stellar ages are estimated. None the less, limitations exist to precisely estimate stellar ages through isochrone fitting, given the complexity and strong non-linearity in the process of finding the solution. Therefore, the usage of independent methods such as gyrochronology as well as probing lithium abundances have been used to increase the confidence on the age limits.

We probed gyro-ages from empirical models by Barnes (2007, hereafter B07) and Mamajek & Hillenbrand (2008, hereafter M08) against our measured photometric projected stellar rotation $P_{\rm rot}$ from Section 3.1. The models provide ages as a function of rotation period and $B - V$ colour, from which NGTS-33 is placed between 17 and 41 Myr according to M08 and B07 models, respectively, assuming $P_{\rm rot}$ from Table 4. However, in the case of the seco$^{\rm nd}$ highest peak of ∼ 0.8 d, which is present in some of the *TESS* sectors (see Section 3.1), the gyro-ages from M08 and B07 would be about 24 and 58 Myr, respectively.

Membership of a star within a cluster or association can allow for more precise constraints to be placed on its bulk properties such as age and metallicity, through an ensemble analysis of all stars in the same group. Using GAIA DR2 data, NGTS-33 was highlighted by Cantat-Gaudin et al. (2019) as a likely member (71 per cent likelihood) of Population V in the young Vela–Puppis region, a cluster of stars with similar kinematics which sit nearby the large Vela OB2 association. Through comparison to PARSEC isochrones ($Z = 0.019$) this population was found to have an age of ∼ 20–35 Myr, further supporting the younger age derived from gyrochronology. Such youth is also supported by NGTS-33 also being included in the selection of young upper main-sequence stars derived by Zari et al. (2018), however, a precise age for this star was not given in this work.

[4]https://github.com/msotov/SPECIES

Table 5. Planetary properties for NGTS-33b.

Property	Value
P (d)	2.827 972 ± 0.000 001
T_c (BJD$_{\rm TDB}$)	2459 986.4090 ± 0.0003
T_{14} (h)	2.62 ± 0.02
a/R_s	6.99 ± 0.07
R_p/R_s	0.1146 ± 0.0004
b	0.74 ± 0.01
i(deg)	83.94 ± 0.12
K (m s^{-1})	383^{+25}_{-23}
e	0.0 (fixed)
ω(°)	90 (fixed)
$M_p(M_J)$	3.63 ± 0.27
$R_{Pp}(R_J)$	1.64 ± 0.07
ρ_p (g cm^{-3})	0.19 ± 0.03
a (au)	0.048 ± 0.002
$T^a_{\rm eq}$ (K)	1991 ± 21
Flux (erg s^{-1}cm^{-2})	(3.56±1.53) × 10^9

[a]Assumed zero Bond albedo.

Finally, we searched the NGTS-33 coadded spectrum for any signs of lithium lines as its abundance is associated to young stellar ages. Due to Li volatility with temperature, its abundance is depleted quickly in stellar atmospheres within the first hundred million years of the star lifetime, hence the existence of photospheric Li could place age limits to the star (e.g. see Christensen-Dalsgaard & Aguirre 2018). Li lines were probed across the coadded spectra, particularly around the strong Li resonant doublet at 6707.775 and 6707.926 Å, however, possibly due to the fast-rotating nature of the host, hence high degree of line blending, no clear evidence of Li was detected at the 17 ppt precision around the doublet. Therefore, although ARIADNE's age of 0.14 ± 0.12 Gyr is in agreement to other dating methods, we adopted an age upper limit of ∼ 50 Myr given the evidence from the literature (Zari et al. 2018; Cantat-Gaudin et al. 2019), the agreement with ARIADNE age estimate as well as our analysis based on gyrochronology. A lower age limit of ∼ 10 Myr is based on planet structure models is discussed in Section 4.2.

3.3 Global modelling

We performed the global modelling with the *emperor* code[5] (Vines Pena & Jenkins 2023, in preparation), a PYTHON toolkit that allows for a joint RV and photometric analysis. *EMPEROR* is equipped with Gaussian Processes as well as autoregressive integrated moving average (ARIMA) models that can be added to the cost function as part of the noise model to properly account for both instrumental and/or astrophysical noise. Moreover, *EMPEROR* flexibility allows the user to choose amongst samplers such as the Markov chain Monte Carlo (MCMC; Foreman-Mackey et al. 2013), parallel tempering MCMC, and nested sampling (*dynesty*; Speagle 2020) to effectively explore the n dimensional parameter space, and reach the optimal solution.

Here, we lay out the steps leading to the adopted solution shown in Tables 4 and 5. We started by running the code with photometry and RV time-series separately, and found a period difference between the data sets of only ∼ 8 min. For the global model, multiples runs were executed to probe the prior distributions, the inclusion of an ARIMA model or Gaussian Processes as part of the noise model,

[5]https://github.com/ReddTea/astroEMPEROR

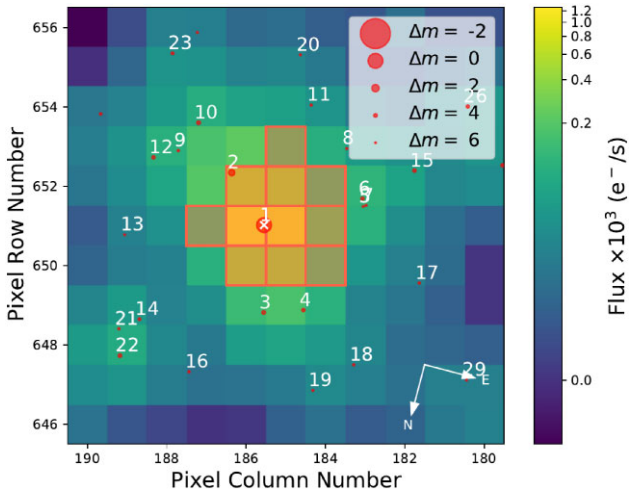

Figure 7. *TESS* Sector 7 full-frame image cutout (11 × 11 pixels) generated with the `tpfplotter` script described in Aller et al. (2020). NGTS-33b is shown in the centre labelled number 1, followed by UCAC4 271-014742 (number 2), a $V = 13.9$ mag, and 32 arcsec away from the planet. Our analysis has shown that the star did not contribute significant flux to the aperture, thus negligible dilution was observed in *TESS*.

linear or quadratic acceleration terms. The adopted solution has been selected upon comparison of every run logarithm Bayesian evidence ($\log Z$) as well as their Bayesian information criteria (BIC). Both metrics are frequently used in model selection, where higher $\log Z$ and lower BIC values indicate a preference for a particular model.

As both photometry and RV measurements are commonly impacted by (non-) correlated noise related to the instruments (e.g. nightly drifts, atmospheric turbulence, so forth) and/or the star (e.g. convective overflows, granulation, flares, and spots), we found that the runs with GPs included in the photometry time-series yielded low BICs and high $\log Z$ compared to the runs without GPs. In fact, NGTS-33 photometry presented clear signs of periodically modulated activity (see Section 3.1) near 0.67 d, thus it was necessary to include a global GP Matern kernel to properly model the spot modulated light curve. We have also allowed supersampling on the transit model with 20 points per bin for the *TESS* Sector 7 to account for its 30 min cadence. The generalized Lomb–Scargle (GLS) periodogram applied to the RV time-series did not show any significant peak at the rotation period, but a highest peak at the planet period 1.83 d (FAP = ∼ 0.1 per cent) followed by the 1.39 d peak (FAP = ∼ 8 per cent), with the latter closer to the first harmonic of the rotation period. Although we are convinced the signal is related to stellar activity, we searched the light curves for any evidence of companions and also computed NGTS-33b TTVs, where both analyses were against further companions in the system. Finally, we tested the dynamical stability (in Section 3.5) assuming a planetary nature for the 1.39 d signal, with results consistent with an unstable system, thus we conclude this signal is indeed related to activity, which was modelled with an additional Keplerian function.

Finally, we point out that no dilution terms have been included in the photometry. The brightest ($V = 13.9$ mag) nearby object, UCAC4 271-014742 is 32 arcsec away and did not affect the transits in the NGTS time-series given its small pixel scale of ∼ 5 arcsec pixel^{-1}. The *TESS* full-frame images though, with an on-sky size of ∼ 21 arcsec, would place the contaminant at ∼ 1.5 pixels away, leading to a theoretical upper limit flux dilution of 8.75 per cent (Fig. 7), had the contaminant been in the same pixel. However, NGTS and *TESS* transits have the same depth, thus we conclude that the transits from the *TESS* mission are not severely affected by dilution. As part of the dilution analysis, we checked our target and the contaminant time-series from NGTS photometry, and ascertain that the transits are on-target. Figs 1 and 2 show the NGTS and *TESS* detrended light curves with their best-fitting models. The RVs are shown in Fig. 3. The parameters of the adopted best-fitting transit and Keplerian models can be found in Table 5, while the second Keplerian associated to stellar activity is in Fig. A1 with parameters shown in Table A2.

We note that two CORALIE RVs highlighted in red squares near phases –0.3 and +0.45 located below and above the curve, respectively, disagree significantly with the model. We investigated their BIS, FWHM–CCF as well as the Hα, Na, Ca line activity indicators and found no evidence that the RVs were affected by stellar activity, thus we kept the points while performing the global modelling.

3.4 Transit-timing variation

TTVs (Agol et al. 2005) occur when mid-transit times T_0 deviate from a linear ephemeris model given by $T_n = T_0 + N \times P$, with N and P being the transit number and orbital period, respectively. The most commonly reported scenarios in the literature are (1) dynamical interactions between the star and the planet, which often results in orbital angular momentum exchanges, leading to orbital decay, and consequently the planet in-falls towards its host star (e.g. WASP-12 Wong et al. 2022). (2) Planet–planet interactions, specifically near mean motion resonance (MMRs) sites, where the interaction becomes more significant, leading to higher TTV amplitudes (e.g. WASP-47 Becker et al. 2015). In addition, the interacting bodies frequently show anticorrelated TTVs and transit duration variations. In fact, several multiplanet systems in MMRs from the *Kepler* mission were validated as bonafide planets through the TTV method (Cochran et al. 2011; Steffen et al. 2012b; Gillon et al. 2017), as the host stars brightness was too dim to allow for the necessary RV precision for mass measurements. However, a few systems had their masses estimated from RVs (Barros et al. 2014; Almenara et al. 2018), while others had their masses and eccentricities measured given the precise TTVs data (Lithwick, Xie & Wu 2012), which revealed the chopping effect, responsible for breaking the M–e degeneracy. Finally, TTVs coupled with RV observations support that HJs are not part of multiplanet systems (Steffen et al. 2012a; Holczer et al. 2016), with such results placing major constraints on giant planets orbital evolution.

NGTS-33b TTVs were estimated from the GP detrended *TESS* and NGTS time-series using only transits with full coverage. Each transit mid-time T_n was modelled with the BATMAN (Kreidberg 2015) code and final distributions computed with the affine invariant MCMC code implemented in the EMCEE package (Foreman-Mackey et al. 2013). The transit depth $p = \frac{R_b}{R_*}$, normalized semimajor axis $a = \frac{a}{R_*}$ and a linear offset bl around the normalized flux were free parameters in the model. T_n, p, and a were assigned the following uniform priors $\mathcal{U}(T_n - 0.1, T_n + 0.1)$, $\mathcal{U}(p - 0.05, T_n + 0.05)$, $\mathcal{U}(a - 0.5, a + 0.5)$, and $\mathcal{U}(bl - 0.1, bl + 0.1)$, respectively, with all other parameters being fixed to their medians from Table 5. Finally, a linear ephemeris model was fit to the T_n, where we used 10 000 MCMC steps, with 20 per cent discarded as burn-in. The best-fitting linear model parameters T_0 and P for *TESS* are given by $T_0 = 1493.2406 \pm 0.0003$ d and $P = 2.827\,96937 \pm 0.000\,00089$ d, while for NGTS $T_0 = 1838.2528 \pm 0.0005$ d and $P = 2.827\,9711 \pm 0.000\,0049$ d. The OC residuals to the linear ephemeris model for both instruments is shown in Fig. 8,

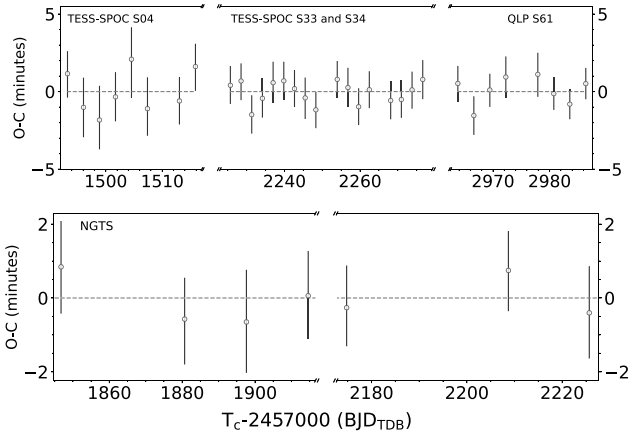

Figure 8. NGTS-33 TTV for the *TESS* mission (top panel; black open circles) and NGTS mission (bottom panel). The abscissa was zoomed for better visualization and avoid the large gaps in the time domain. In the top panel, each portion represents a *TESS* sector with its corresponding reduced pipeline and sector.

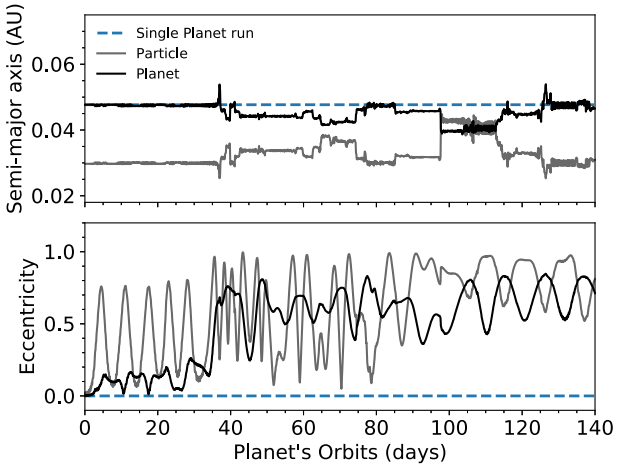

Figure 9. Top panel: semimajor axis evolution for NGTS-33 with two planets at orbital periods consistent with NGTS-33b (in black) and a particle similar to a Jupiter planet with $m \sin i = 1.29\,M_J$ at 1.39 d (in grey). The dashed blue line corresponds to the orbital evolution of the semimajor axis for when NGTS-33b is alone in the system. Bottom panel**:** eccentricities evolution. Colours and labels are the same as shown in the top panel.

where no evidence for significant TTVs was found, and data made available in Table A3.

3.5 NGTS-33 DYNAMICAL STABILITY

Our global model analysis (Section 3.3) revealed a planet signal at 2.83 d and rotation signals at 0.67 and 0.8 d from the photometric time-series. The RV data set shows the planet signal followed by an additional peak at 1.39 d, which is twice the photometric rotation period, thus we attributed to stellar activity. In order to provide further credibility that the 1.39 d signal is activity related, we performed dynamical stability simulations to initially (1) assure our solution is dynamically stable and also (2) reject the planetary nature of the 1.39 d signal detected in the RV periodogram. For this purpose, we used *REBOUND*[6] (Rein & Liu 2012), an *N*-body problem solver that integrates particles' motion in time under the influence of larger bodies gravitational potential.

Anchored on our orbital solution laid out in Section 3.3 and shown in Table 4, we ran the code up to $\sim$ 100 Myr assuming a two-body problem made up of our host star and NGTS-33b in order to test the systems stability given our solution. We found no significant changes in its orbital parameters up to this time, otherwise, a larger integration time would have been carried out. Therefore, we stopped the run and assumed the orbital solution is dynamically stable up to $\sim$ 100 Myr.

In the second scenario containing the host star, NGTS-33b, and an inner test particle consistent with the RV signal, i.e. orbital period of 1.39 d and 1.29 M_J. Fig. 9 showed that the semimajor axes and eccentricities were dynamically unstable, with the particle and planet reaching an eccentricity of 1.0 after nearly 140 orbits of NGTS-33b, thus the integration had been stopped due to the chaotic motion. As the particle inclination is unknown, we ran the code multiple times for a 60°–85° inclination grid with 5° steps. Every run resulted in the system being unstable. For simulations with nearly co-planar orbits, the planet would have likely been detected during our searches for further planets in the photometric time-series. We point out that chaotic simulations are highly sensitive to the initial conditions, i.e. a change in the particle's parameters result in a slight distinct orbital solution, yet every instance yielded unstable parameters, with the particle frequently being ejected at some point in time. Such chaotic behaviour is expected as both NGTS-33b and the particle are HJs near MMRs. Finally, we conclude that our solution described in the global model is dynamically stable, with the second Keplerian being interpreted as stellar activity, rather than an HJ near an MMR state, which is corroborated by the non-TTV detection in Section 3.4.

4 DISCUSSION

4.1 The transiting hot Jupiter population

Here, we place NGTS-33 planetary system in context with the THJ population drawn from the TEPCat catalogue (Southworth 2011). We selected the planets by $P \leq 10$ d and mass range $0.1 \leq M \leq 13\,M_J$, yielding 558 giant planets[7] on 2024 May 2. Our analysis laid out in Section 3 reveals that NGTS-33 is not only the first NGTS discovery of a super-Jupiter around a young fast-rotating host, but also the lowest in density around hot stars ($T_{\rm eff} \geq 6900$ K), thus making it an interesting target for transmission and emission spectroscopy follow-up with the *JWST* (see Section 4.3).

Fig. 10 top panel shows the cumulative mass distribution function for the THJ sample, with NGTS-33b belonging to the $\sim$ 7 per cent most massive THJs discoveries thus far. If we compare it to the scarce population of $\sim$ 11 massive THJ around hot hosts, shown in the embedded plot at the lower right, NGTS-33b is amongst the seco[nd] most massive THJ detected, alongside planets such as MASCARA-1 (Talens et al. 2017), HAT-P-69 (Zhou et al. 2019), and OGLE-TR-L9 (Snellen et al. 2009), with masses of $M_p = 3.7 \pm 0.1$, 3.6 ± 0.6, and $= 4.5 \pm 1.5\,M_J$, respectively. We note that NGTS-33b mass is in 1σ agreement to them, thus placing it amongst the most massive planets around hot hosts. On the other hand, the lower panel of Fig. 10 shows the hosts $T_{\rm eff}$ cumulative distribution function. The rapid growth of the slope centred around G dwarfs and spread over K-type ($\sim$ 4000–5250 K) through late F-type stars ($\sim$ 6300 K) represents the majority

[6] https://rebound.readthedocs.io/en/latest/

[7] We do not include HATS-70 in the analysis as it is at the boundary between planets and brown dwarfs, with a mass upper limit at 1σ of 13.02 M_J.

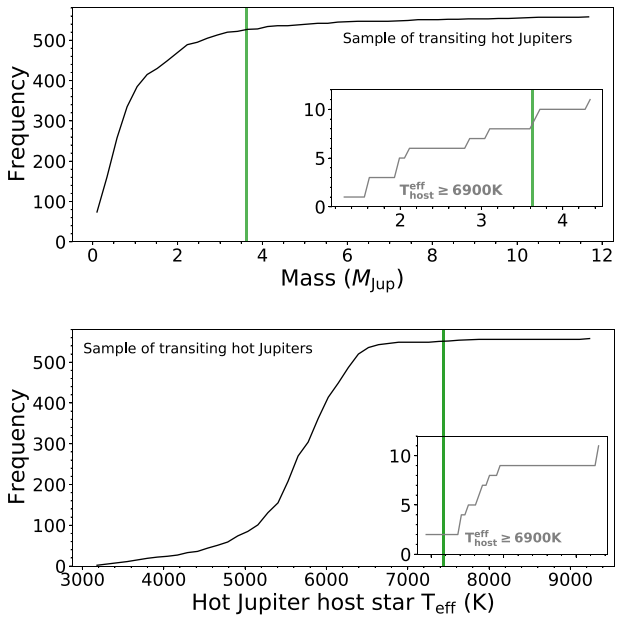

Figure 10. Top panel: cumulative distribution functions for the sample of THJs shown as a black solid curve. The green vertical bar highlights NGTS-33b's mass. The bottom right plot shows a slice of the cumulative distribution (in grey) containing HJs whose host effective temperatures are above 6900 K. NGTS-33b is not included in either plot. Bottom panel: same as above for the effective temperatures of THJ hosts.

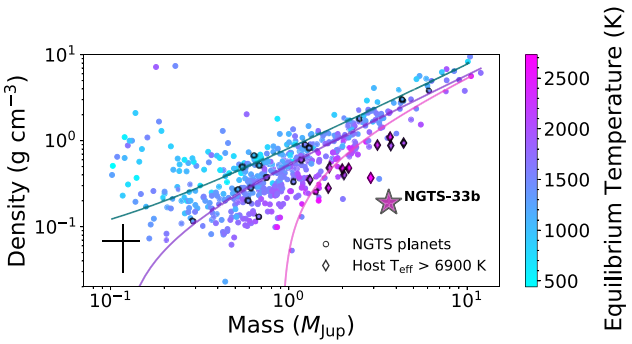

Figure 11. THJ bulk densities as a function of their masses, colour coded by equilibrium temperature. NGTS-33b is represented by the large red star near the image centre towards the bottom right, while the typical uncertainties are shown as a black cross in the bottom left panel. Black-edged diamonds and circles highlight the THJs whose host T_{effs} are greater than 6900 K, and the population of NGTS detected planets, respectively. Best-fitting empirical linear models describing the THJ populations with distinct T_{eq} are highlighted by the cyan, purple, and pink colours. See Section 4.1 for explanation.

of THJ hosts. NGTS-33 is highlighted by the green vertical bar, and is amongst the ∼2 per cent most massive planet hosts, thus reinforcing the rarity of NGTS-33b detection.

In Fig. 11, we compared NGTS-33b's bulk density with the THJ population, highlighting other NGTS discoveries as well as giants around as hot hosts ($T_{\rm eff} \geq 6900$ K; shown as diamonds in the figure). The $\rho_{\rm p}$ median of similar planets ($2 \leq M \leq 5\,M_{\rm J}$) is ~ 1.48 g cm^{-3}, thus placing NGTS-33b's density ∼ 13 per cent below the median, or ∼ 22 per cent less dense, if compared to the $\rho_{\rm p}$ median (0.88 g cm^{-3}) of THJ hosted by stars with $T_{\rm eff} \geq 6900$ K. Such discrepancies may be attributed to NGTS-33b not having undergone significant gravitational collapse due to its young age, thus evidenced by its large radius. However, an irradiated atmosphere, tidal heating during its orbital circularization or a combination of both could lead to an increase in its radius (see Section 4.2), thus significantly reducing its bulk density compared to giants with similar mass.

Finally, in the same figure, distinct THJ groups are observed, which can be distinguished by their $T_{\rm eq}$ and evidenced by the colour gradient. The THJs with higher $T_{\rm eq}$ have significantly lower $\rho_{\rm p}$ compared to cooler planets, thus providing evidence that their bulk densities are a function of $T_{\rm eq}$ regardless of their thermal evolution processes (e.g. high stellar incidences, tidal heating, so forth). For all planetary masses, the $T_{\rm eq}$ correlates positively with radius, even though more massive planets should be less affected by radius anomaly. This is evidenced by the increasing bulk density with lower $T_{\rm eq}$ regardless of mass bin. A thorough analysis of the $T_{\rm eq}$, $M_{\rm p}$ versus $\rho_{\rm p}$ parameter space may even serve as an independent means to estimate planetary radius for non-transiting planets, where their masses, temperatures could be used to estimate a bulk density, and subsequently their radius. A complete analysis of this problem is beyond the scope of this work, however, we performed a linear fit assuming three THJ populations defined by $T_{\rm eq}$ bins. The lower and upper boundaries were initially motivated by visual inspection, but corroborated by several works showing that the radius anomaly is observed roughly at 1000–1400 K (e.g. Demory & Seager 2011a; Thorngren & Fortney 2018).

Therefore, we adjusted linear empirical models in the form of $\rho_{\rm p} = {\rm A}\times{\rm M} + {\rm B}$ in order to probe the relationship between $\rho_{\rm p}$ and M to the three populations defined by $T_{\rm eq} < 1400$ K (cyan), $T_{\rm eq} \geq 1400$ K and $T_{\rm eq} < 2300$ K (purple), and $T_{\rm eq} \geq 2300$ K (pink), respectively. A and B are free parameters to the model, with best-fitting values given by 0.7706 ± 0.0004 M$_{\rm J}^{-1}$ and 0.045 ± 0.001 g cm^{-3}, 0.586 ± 0.001 M$_{\rm J}^{-1}$ and -0.065 ± 0.004 g cm^{-3}, and 0.5858 ± 0.0001M$_{\rm J}^{-1}$ and -0.537 ± 0.002 g cm^{-3}, respectively, for the three curves defined above by their $T_{\rm eq}$. The cyan and purple models indicate that giants with lower $T_{\rm eq}$ have larger $\rho_{\rm p}$ regardless of mass, with a typical $\rho_{\rm p}$ differences of 0.18, 0.23, and 0.62 g cm^{-3} for giants with masses of 0.6, 1, and 10 M$_{\rm J}$ planets, respectively. Finally, we note that NGTS-33b was not taken into account during the model fitting as its density does not follow any of the three populations.

4.2 Radius inflation

High incidence stellar flux into a planet's gaseous envelope seems to be the main driving mechanism responsible for the HJs radius anomaly. Demory & Seager (2011b) estimate that an incident flux throughput of $\sim 2\times10^5$ Wm^{-2} is required for planetary inflation to become observable. Miller & Fortney (2011) point out that the metallicity fraction (Z) also plays an important role, with higher Z fractions reducing the inflation efficiency. In addition, statistical analysis based on planetary thermal evolution models on a sample of 281 HJs (Thorngren & Fortney 2018) showed that the necessary conversion of incident flux into internal heating required to reproduce HJs observed radii, peak's at equilibrium temperature ($T_{\rm eq}$) ∼ 1500 K. Finally, Hartman et al. (2016) show that HJ radii grows as a function of main-sequence star's fractional ages, i.e. as stars age on the main sequence, they brighten up, thus leading to higher planetary irradiation and hence higher $T_{\rm eq}$ of their orbiting planets. However, alternative scenarios exist to explain HJ radius anomalies, such as star–planet tidal interactions, which lead to internal heating of the planet, thus causing a radius inflation (e.g. see Fortney et al. 2021, for a review).

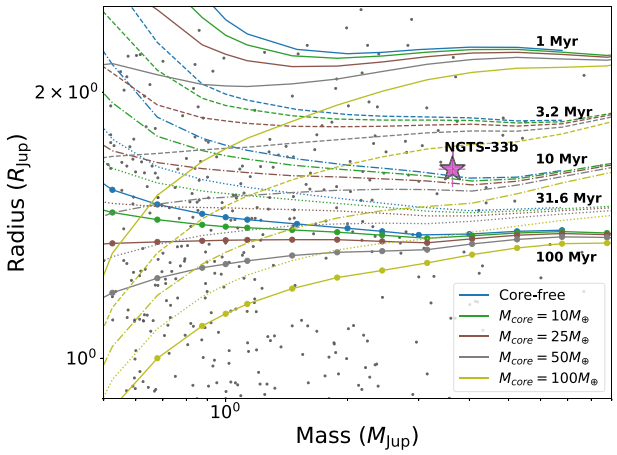

Figure 12. Planet structure models by Fortney, Marley & Barnes (2007). Colour lines represent the same assumed planet core mass, while the lines shapes describes an HJ evolved to a given epoch shown on the right. For instance, the solid lines on the top represent a HJ at 1 Myr, where blue and green lines indicating a core-free and 10 $M_\oplus$ core mass models. NGTS-33b is highlighted by the purple star symbol and black dots are THJs from the TEPCat catalogue.

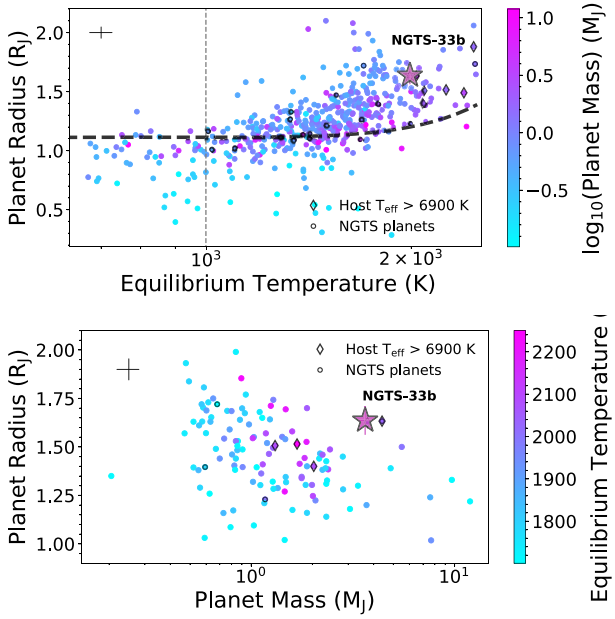

Figure 13. Top panel: equilibrium temperature versus planet radius colour-coded by the logarithm of planet mass. Black-dashed line represents an inflation-free model for an HJ evolved to 4.5 Gyr with an H/He composition adapted from Thorngren & Fortney (2018). NGTS-33b is displayed by the red-coloured star above the model near the image top right. Black cross at the top left corner represents the HJs parameters uncertainties standard deviation, and red open circles marks metal-poor K dwarf stars. Bottom panel: M_p versus R_p colour-coded by T_{eq} showing HJs from the top figure with T_{eq} between 1700 and 2300 K.

We probed inflation levels from planetary structure models by Fortney et al. (2007, hereafter F07). In Fig. 12, we show F07 models converted into the appropriate planet–star distance of $\sim$ 0.02 au and evaluated at the model closest in age to NGTS-33b, which shows that its measured radius is above the expected by $\sim$ 11–15 per cent assuming a core-free and 100 $M_\oplus$ core mass, respectively. Therefore, even at nearly $\sim$ 50 Myr, evolutionary models do not predict such radius, thus, despite its young age, stellar irradiation may be partially contributing to its large size. Had its age been $\sim$10 Myr, NGTS-33b radius would be nearly in agreement to F07 models, hence inflation-free, however, such young age is not corroborated by the gyrochronology and cluster membership analysis (see Section 3.2.1), hence it is unlikely that the planet is younger than $\sim$ 10 Myr given the uncertainties in the models and the systems' parameters. Moreover, the absence of infrared excess in the SED fitting (Fig. 6) provides further evidence on NGTS-33 age lower limit as discs tend to disperse around 5-10 Myrs (Hillenbrand 2005). Therefore, we assume an age lower limit about 10 Myr, and conclude that NGTS-33b large radius is likely attributed to a combination of its very young nature and stellar irradiation, causing a radius inflation of $\sim$ 13 per cent on average.

In Fig. 13 top panel, we compared NGTS-33b to the THJ population in the R_p versus T_{eq} parameter space colour-coded by the logarithm of their masses. The planet's location, shown as a purple star symbol, suggests it is inflated compared to the HJ population as well as its counterparts with similar temperatures (1700 $\leq T_{eq} \geq$ 2300 K). However, we point out that the comparison above is partially affected by the HJ population broad ages. Fig. 13 lower panel highlights the THJs in the T_{eq} range in the R_p versus M_{Jup} phase space, where NGTS-33b stands out as a massive and inflated planet. Such result places NGTS-33b as one of the first young and inflated HJ detected, with only four THJs younger than 100 Myr reported[8] thus far (e.g. K2-33 b, TOI-942 b, CoRoT-20 b, and WASP-33 Ab). Therefore, its discovery will add to the small but growing population of young planets, and subsequent follow-up will help place constraints on the formation and evolution of massive and hot systems.

4.3 Is NGTS-33b suitable for atmospheric follow-up with *JWST*?

The discovery of transiting planets allowed the investigation of their atmospheric abundances, with short-period HJs remaining the best targets for atmospheric follow-up. Their high equilibrium temperature ($Teq \geq 1000$ K) and lower densities ($\rho_p < 0.3$ g cm^{-3}), induces scale heights such that the chemistry of inner layers is brought up, thus allowing the investigation of a variate of species by the transmission spectroscopy technique (Seager & Sasselov 2000). On the other hand, the planet's secondary eclipses allows the inference of day-side temperature as well as the albedo/reflectivity through emission spectroscopy. Such techniques have been vastly applied by ground- (e.g. ESPRESSO/VLT and HIRES/Keck) and space-based missions such as the *Hubble Space Telescope*, *Spitzer*, and recently, the *JWST*.

Stevenson et al. (2016) selected 12 objects for *JWST* follow-up dubbed community targets (CTs) based mostly on their properties, where optimal candidates are often quiet ($\log R'_{HK} \leq -4.8$), short period ($P < 10$ d), bright ($J < 10.5$ mag) and have orbital solutions and masses well constrained. A high ecliptic latitude ($b > 45^\circ$) is also important as such targets being near or within the continuing viewing zone allow for multiple visits, consequently a higher SNR would be reached. Since NGTS-33b matches several of these criteria, we computed its signal size per scale height defined in Kempton et al. (2018) by assuming a cloud-free atmosphere and constant T_{eq}, which

[8] https://exoplanet.eu/

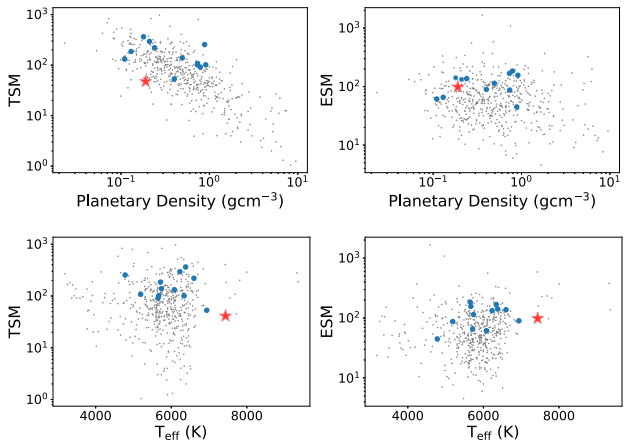

Figure 14. Top panel: TSM and ESM as a function of planetary density for the THJ sample are shown in black circles, whereas *JWST* community targets by Stevenson et al. (2016) are marked by blue circles. NGTS-33b is represented by the big red star. The TSM and ESM were computed homogeneously using the systems properties from the TEPCat catalogue. Bottom panel: TSM and ESM as a function of host effective temperature. Colour schemes are the same as described in the top panel.

is given by

$$\Delta D = \frac{2k_{\rm B}T_{\rm eq}R_{\rm p}}{\mu g R_{\rm S}^2} \tag{3}$$

with $k_{\rm B}$, μ, and g being the Boltzmann constant, mean molecular weight and the planet's gravity. From equation (3), we estimated NGTS-33b ΔD of $\sim$ 53 ppm H^{-1}, which is comparable to the lower limit of the CT signal size range of 60–240 ppm H^{-1}, thus making NGTS-33b an interesting target for follow-up observations.

We have also computed the transmission and emission spectroscopy metrics (TMS and EMS) homogeneously from equations (1) and (4) by Kempton et al. (2018) shown in Fig. 14. Although NGTS-33b seems less favourable for transmission spectroscopy as compared to the HJs and CT targets at similar densities (top left panel), its host sits in an under populated part of the TSM versus $T_{\rm eff}$ parameter space (bottom left panel), thus making the system an interesting candidate for atmosphere characterization. In addition, the hosts with $T_{\rm eff} > 6900$ K, mostly left of NGTS-33 are orbited by denser planets ($\rho_{\rm p} > 0.28$ g cm^{-3}), hence distinct atmospheric properties/abundances given their smaller scale heights. The ESM though indicates that NGTS-33b is an interesting target for *JWST* emission spectroscopy follow-up as its ESM is equivalent to CT and above most of HJ ESMs (top right panel). Similarly to the TSM, ESM versus $T_{\rm eff}$ shows that very few stars populate the hot edge ($T_{\rm eff} > 6900$ K) of the parameter space. Even though a handful of them ($\sim$ 4 out of 11) have been targeted for follow-up, the majority lacks atmospheric characterization. Therefore, such part of the parameter space remains a golden region for an in-depth *JWST* atmospheric follow-up.

4.4 NGTS-33b obliquity follow-up

When a transiting planet blocks part of the stellar disc, the spectral line centroids can be shifted, leading to an RV anomaly, well known as the Rossiter–McLaughlin effect (RM; Triaud et al. 2009). Such phenomenon allows us to measure the obliquity angle between the planet's orbital axis to that of the star. In fact, the technique was responsible to reveal that a handful of close-in massive giants have non-zero obliquities (e.g. KELT-17b, MASCARA-1b, and TOI-1431b), with some even in retrograde orbits (HAT-P-14b; Winn et al. 2011). In addition, Winn et al. (2011) point that cool hosts tend to have planets with low obliquities, compared to hot hosts, hence indicating that even THJs may have undergone distinct migration channels, yet non-zero obliquities could have also been a result of primordial misalignment between the central star and its protoplanetary disc (Albrecht, Dawson & Winn 2022). Therefore, measuring the obliquity of NGTS-33b might provide valuable information on massive planetary systems evolution history.

The relatively large star-to-planet radius ratio and the host fast-spinning rate indicates that NGTS-33 is a good candidate for in-transit RV monitoring. The RM amplitude can be estimated by

$$A_{\rm RM} = \frac{2}{3}\left(\frac{R_{\rm p}}{R_*}\right)^2 v \sin i_* \sqrt{1-b^2}, \tag{4}$$

where b is the planet's impact parameter. An $A_{\rm RM}$ $\sim$660.56 ms^{-1} is expected for the planet, assuming $v \sin i_* \sim 111.87$ km s^{-1} from $P_{\rm rot}$ and $R_{\rm p}$. Such value is $\sim$ 1.7 higher than the planet-induced RVs, which is explained by the relatively large coverage of the stellar disc by the planet, but mainly due to the star's extremely short rotation period of 0.67 d. In addition, the system's obliquity could possibly be measured directly through Doppler tomography (Cameron et al. 2010; Watanabe et al. 2022). Finally, Gaudi & Winn (2007) showed that, for small planets of mass M on an edge-on circular orbit with period P, the ratio between the RM amplitudes and that of the planet induced velocity can be approximated by

$$\frac{A_{\rm RM}}{K} \sim 0.3 \left(\frac{M}{M_{\rm Jup}}\right)^{-1/3} \left(\frac{P}{3\ {\rm d}}\right)^{1/3} \left(\frac{v \sin i_*}{5\ {\rm km\ s^{-1}}}\right). \tag{5}$$

Using our derived values for M, P, and $v \sin i_*$, we would expect an even larger ratio of about 4.3. None the less, NGTS-33b's RM effect is expected to be above the planet's induced velocity, thus it can easily be measured with high-resolution spectrographs ($R \geq$ 60 000).

5 CONCLUSION

We report the discovery of NGTS-33b, a super-Jupiter with mass, radius, and bulk density of 3.63 $\pm$ 0.27 M$_{\rm J}$, 1.64 $\pm$ 0.07 R$_{\rm J}$, and 0.19 $\pm$ 0.03 g cm^{-3}, respectively. The planet orbits a massive A9V star every 2.83 d, whose mass, radius and effective temperature are of 1.60 $\pm$ 0.11 M$_{\rm s}$, 1.47 $\pm$ 0.06 R$_{\rm s}$, and 7437 $\pm$ 72 K, respectively. NGTS-33 is one of the youngest hosts discovery thus far, having an age of 10–50 Myr, and the fifth hottest star hosting a THJ. In addition, membership analysis indicates that NGTS-33 may be part of the Vela OB2 association. In fact, NGTS-33 is not only young but also rare, laying amongst the 2 per cent most massive THJ hosts, whereas the planet represents the $\sim$ 7 per cent most massive THJs currently detected. Moreover, planetary structure models show that NGTS-33b's radius is likely inflated by up to $\sim$ 15 per cent. Such is evidenced by its extremely low density compared to THJ of similar M and $T_{\rm eq}$. In fact, NGTS-33b's bulk density is nearly 13 per cent lower than that expected for its mass, thus likely a combination of its large radius due to youth and its irradiated atmosphere. In addition, we noticed what may be three populations of THJs distinguished by their $T_{\rm eq}$, with boundaries at $T_{\rm eq} \sim$ 1400 and $\sim$ 2300 K. Giants with $T_{\rm eq} <$ 1400 K were found to have larger $\rho_{\rm p}$ independent of mass, thus implying that their $\rho_{\rm p}$ are, to first order, a function of $T_{\rm eq}$ regardless of thermal evolution processes. Empirical linear models fitted to cooler ($T_{\rm eq} <$ 1400 K) and warmer (1400 $\leq T_{\rm eq} <$2300 K) giants populations

showed a difference in ρ_p of about 0.18, 0.23, and 0.62 g cm^{-3} for giants with masses of 0.6, 1 and 10 M_J planets, respectively.

The ESM computed for NGTS-33b puts it near the *JWST* CTs boundary, and one of the lowest in density amongst hot hosts, thus making it a suitable candidate for emission spectroscopy with *JWST*. Additionally, NGTS-33's fast spin combined with the planet's large radius, gives it an expected RM amplitude of ~ 660.56 m s^{-1} , i.e. 1.7 times that of the RV-induced variation generated by the planet, thus making it a good candidate for obliquity studies also.

Finally, with only 11 detections thus far, the number of massive Jupiters hosted by hot stars ($T_{\rm eff} \geq 6900$ K) is strikingly scarce, thus the discovery of NGTS-33b will significantly add to the small but increasing population of massive THJs, which will help place further constraints on current formation and evolution models for such planetary systems.

ACKNOWLEDGEMENTS

Based on data collected under the NGTS project at the ESO La Silla Paranal Observatory. The NGTS facility is operated by the consortium institutes with support from the UK Science and Technology Facilities Council (STFC) under projects ST/M001962/1, ST/S002642/1, and ST/W003163/1. This study is based on observations collected at the European Southern Observatory under ESO programme 105.20G9. DRA acknowledges support of ANID-PFCHA/Doctorado Nacional-21200343, Chile, and thank the anonymous referee for the useful comments that improved the quality of this work. JSJ gratefully acknowledges support by FONDECYT grant 1240738 and from the ANID BASAL projects ACE210002 and FB210003. JIV acknowledges support of CONICYT-PFCHA/Doctorado Nacional-21191829. Contributions at the University of Geneva by ML, FB and SU were carried out within the framework of the National Centre for Competence in Research 'PlanetS' supported by the Swiss National Science Foundation (SNSF). The contributions at the University of Warwick by PJW, SG, DB, and RGW have been supported by STFC through consolidated grants ST/P000495/1 and ST/T000406/1. The contributions at the University of Leicester by MGW and MRB have been supported by STFC through consolidated grant ST/N000757/1.

CAW acknowledges support from the STFC grant ST/P000312/1. TL was also supported by STFC studentship 1226157. MNG acknowledges support from the European Space Agency (ESA) as an ESA Research Fellow. This project has received funding from the European Research Council (ERC) under the European Union's Horizon 2020 research and innovation programme (grant agreement No 681601). The research leading to these results has received funding from the European Research Council under the European Union's Seventh Framework Programme (FP/2007-2013)/ERC Grant Agreement n. 320964 (WDTracer). The contributions of ML and MB have been carried out within the framework of the NCCR PlanetS supported by the Swiss National Science Foundation under grants 51NF40_182901 and 51NF40_205606. ML also acknowledges support of the Swiss National Science Foundation under grant number PCEFP2_194576.

DATA AVAILABILITY

The data underlying this article are made available in its online supplementary material.

REFERENCES

Agol E., Steffen J., Sari R., Clarkson W., 2005, MNRAS, 359, 567
Albrecht S. H., Dawson R. I., Winn J. N., 2022, PASP, 134, 082001
Alibert Y., Mordasini C., Benz W., Winisdoerffer C., 2005, A&A, 434, 343
Allard F., Homeier D., Freytag B., 2012, Phil. Trans. R. Soc. A, 370, 2765
Aller A., Lillo-Box J., Jones D., Miranda L. F., Forteza S. B., 2020, A&A, 635, A128
Almenara J. M. et al., 2018, A&A, 615, A90
Alves D. R. et al., 2022, MNRAS, 517, 4447
Auvergne M. et al., 2009, A&A, 506, 411
Bakos G., Noyes R., Kovács G., Stanek K., Sasselov D. D., Domsa I., 2004, PASP, 116, 266
Bakos G. et al., 2010, ApJ, 710, 1724
Barbato D. et al., 2019, A&A, 621, A110
Barnes S. A., 2007, ApJ, 669, 1167 (B07)
Barros S. et al., 2014, A&A, 561, L1
Battley M. et al., 2024, A&A, 686, A230
Bayliss D. et al., 2018, MNRAS, 475, 4467
Bayliss D. et al., 2022, X-Ray, Optical, and Infrared Detectors for Astronomy X, SPIE, Montréal, Québec, Canada, p. 441
Becker J. C., Vanderburg A., Adams F. C., Rappaport S. A., Schwengeler H. M., 2015, ApJ, 812, L18
Borucki W. J. et al., 2010, Science, 327, 977
Bouchy F. et al., 2024, A&A, 684, A201
Bouma L., Hartman J., Bhatti W., Winn J., Bakos G., 2019, ApJS, 245, 13
Brahm R., Jordán A., Espinoza N., 2017, PASP, 129, 034002
Brown A. G. et al., 2021, A&A, 649, A1
Bryant E. M. et al., 2020, MNRAS, 499, 3139
Buchhave L. A., Bitsch B., Johansen A., Latham D. W., Bizzarro M., Bieryla A., Kipping D. M., 2018, ApJ, 856, 37
Caldwell D. A. et al., 2020, Res. Notes AAS, 4, 201
Cameron A. C. et al., 2010, MNRAS, 407, 507
Cantat-Gaudin T. et al., 2019, A&A, 626, A17
Castelli F., Kurucz R. L., 2004, preprint (astro-ph/0405087)
Charbonneau D., Brown T. M., Latham D. W., Mayor M., 2000, ApJ, 529, L45
Chazelas B. et al., 2012, Ground-based and Airborne Telescopes IV, SPIE, Amsterdam, Netherlands, p. 84440E
Christensen-Dalsgaard J., Aguirre V. S., 2018, preprint (arXiv:1803.03125)
Cochran W. D. et al., 2011, ApJS, 197, 7
Collier Cameron A. et al., 2006, MNRAS, 373, 799
Cubillos P., Harrington J., Loredo T. J., Lust N. B., Blecic J., Stemm M., 2016, AJ, 153, 3
Demory B.-O., Seager S., 2011a, ApJS, 197, 12
Demory B.-O., Seager S., 2011b, ApJS, 197, 12
Des Etangs A. L. et al., 2010, A&A, 514, A72
Dong J., Foreman-Mackey D., 2023, AJ, 166, 112
Fernández Fernández J., Wheatley P. J., King G. W., Jenkins J. S., 2024, MNRAS, 527, 911
Fischer D. A., Valenti J., 2005, ApJ, 622, 1102
Foreman-Mackey D., Hogg D. W., Lang D., Goodman J., 2013, PASP, 125, 306
Fortney J. J., Marley M. S., Barnes J. W., 2007, ApJ, 659, 1661 (F07)
Fortney J. J., Dawson R. I., Komacek T. D., 2021, J. Geophys. Res. Planets, 126, e2020JE006629
Gaudi B. S., Winn J. N., 2007, ApJ, 655, 550
Gill S. et al., 2024, MNRAS, 533, 109
Gillen E. et al., 2020, MNRAS, 492, 1008
Gillon M. et al., 2017, Nature, 542, 456
Gonzalez G., 1997, MNRAS, 285, 403
Hartman J. D. et al., 2016, AJ, 152, 182
Hauschildt P. H., Allard F., Baron E., 1999, ApJ, 512, 377
Henden A. A., Levine S., Terrell D., Welch D. L., 2015, American astronomical society meeting abstracts# 225. p. 336
Hidalgo S. L. et al., 2018, ApJ, 856, 125
Hillenbrand L. A., 2005, preprint (astro-ph/0511083)

Hirano T., Sanchis-Ojeda R., Takeda Y., Winn J. N., Narita N., Takahashi Y. H., 2014, ApJ, 783, 9
Holczer T. et al., 2016, ApJS, 225, 9
Hoyer S. et al., 2023, A&A, 675, A81
Hsu D. C., Ford E. B., Ragozzine D., Ashby K., 2019, AJ, 158, 109
Husser T.-O., Wende-von Berg S., Dreizler S., Homeier D., Reiners A., Barman T., Hauschildt P. H., 2013, A&A, 553, A6
Jenkins J. et al., 2009, MNRAS, 398, 911
Jenkins J. M. et al., 2016, Proc. SPIE, 9913, 99133E
Jenkins J. S. et al., 2017, MNRAS, 466, 443
Jenkins J. S. et al., 2020, Nat. Astron., 4, 1148
Johnson J. A., Aller K. M., Howard A. W., Crepp J. R., 2010, PASP, 122, 905
Jones M. et al., 2016, A&A, 590, A38
KURUCZ R.-L., 1993, Kurucz CD-Rom, 13
Kaufer A., Stahl O., Tubbesing S., Nørregaard P., Avila G., Francois P., Pasquini L., Pizzella A., 1999, The Messenger, 95, 8
Kempton E. M.-R. et al., 2018, PASP, 130, 114401
Kovács G., Zucker S., Mazeh T., 2002, A&A, 391, 369
Kreidberg L., 2015, PASP, 127, 1161
Kreutzer L. T., Gillen E., Briegal J. T., Queloz D., 2023, MNRAS, 522, 5049
Kunimoto M. et al., 2021, Res. Notes AAS, 5, 234
Lightkurve Collaboration et al., 2018, Astrophysics Source Code Library, record ascl:1812.013
Lithwick Y., Xie J., Wu Y., 2012, ApJ, 761, 122
Lopez E. D., Fortney J. J., 2013, ApJ, 776, 2
Lovis C., Pepe F., 2007, A&A, 468, 1115
McCormac J. et al., 2017, PASP, 129, 025002
McCormac J. et al., 2020, MNRAS, 493, 126
McQuillan A., Mazeh T., Aigrain S., 2014, ApJS, 211, 24
Mamajek E. E., Hillenbrand L. A., 2008, ApJ, 687, 1264 (M08)
Mayor M., Queloz D., 1995, Nature, 378, 355
Mayor M. et al., 2003, The Messenger, 114, 20
Miller N., Fortney J. J., 2011, ApJ, 736, L29
Morton T. D., 2015, Astrophysics Source Code Library, record ascl:1503
Mulders G. D., Pascucci I., Apai D., 2015, ApJ, 798, 112
O'Brien S. M. et al., 2022, MNRAS, 509, 6111
Osborn A., Bayliss D., 2020, MNRAS, 491, 4481
Owen J. E., Wu Y., 2017, ApJ, 847, 29
Pepe F., Mayor M., Galland F., Naef D., Queloz D., Santos N., Udry S., Burnet M., 2002, A&A, 388, 632
Piso A.-M. A., Youdin A. N., 2014, ApJ, 786, 21
Pollacco D. L. et al., 2006, PASP, 118, 1407
Pollack J. B., Hubickyj O., Bodenheimer P., Lissauer J. J., Podolak M., Greenzweig Y., 1996, icarus, 124, 62
Queloz D. et al., 2000, A&A, 354, 99
Reffert S., Bergmann C., Quirrenbach A., Trifonov T., Künstler A., 2015, A&A, 574, A116
Rein H., Liu S. F., 2012, A&A, 537, A128
Ricker G. R. et al., 2015, J. Astron. Telesc. Instrum. Syst., 1, 014003
Santerne A. et al., 2016, A&A, 587, A64
Santos N., Israelian G., Mayor M., 2001, A&A, 373, 1019
Seager S., Sasselov D. D., 2000, ApJ, 537, 916
Skrutskie M. F. et al., 2006, AJ, 131, 1163
Smith A. et al., 2021, A&A, 646, A183
Smith G. D. et al., 2023, MNRAS, 523, 169
Snellen I. et al., 2009, A&A, 497, 545
Soto M., Jenkins J. S., 2018, A&A, 615, A76
Southworth J., 2011, MNRAS, 417, 2166
Speagle J. S., 2020, MNRAS, 493, 3132
Stassun K. G. et al., 2018, AJ, 156, 102
Steffen J. H. et al., 2012a, Proc. Natl. Acad. Sci., 109, 7982
Steffen J. H. et al., 2012b, MNRAS, 421, 2342
Stevenson K. B. et al., 2016, PASP, 128, 094401
Talens G. et al., 2017, A&A, 606, A73
Tamuz O., Mazeh T., Zucker S., 2005, MNRAS, 356, 1466
Thorngren D. P., Fortney J. J., 2018, AJ, 155, 214
Tilbrook R. H. et al., 2021, MNRAS, 504, 6018
Triaud A. H. et al., 2009, A&A, 506, 377
Valenti J. A., Fischer D. A., 2005, ApJS, 159, 141
VanderPlas J. T., 2018, ApJS, 236, 16
Vick M., Su Y., Lai D., 2023, ApJ, 943, L13
Vidal-Madjar A., Des Etangs A. L., Désert J.-M., Ballester G., Ferlet R., Hébrard G., Mayor M., 2003, Nature, 422, 143
Vines J. I., Jenkins J. S., 2022, MNRAS, 513, 2719
Vines J. I. et al., 2019, MNRAS, 489, 4125
Vines J. I. et al., 2023, MNRAS, 518, 2627
Watanabe N. et al., 2022, MNRAS, 512, 4404
West R. G. et al., 2019, MNRAS, 486, 5094
Wheatley P. J. et al., 2013, in Saglia R., ed., EPJ Web Conf. Vol. 47, Hot Planets and Cool Stars, p. 13002
Wheatley P. J. et al., 2018, MNRAS, 475, 4476
Winn J. N. et al., 2011, AJ, 141, 63
Wong I., Shporer A., Vissapragada S., Greklek-McKeon M., Knutson H. A., Winn J. N., Benneke B., 2022, AJ, 163, 175
Wright E. L. et al., 2010, AJ, 140, 1868
Wyttenbach A. et al., 2020, A&A, 638, A87
Zari E., Hashemi H., Brown A. G. A., Jardine K., de Zeeuw P. T., 2018, A&A, 620, A172
Zhou G. et al., 2019, AJ, 158, 141

SUPPORTING INFORMATION

Supplementary data are available at *MNRAS* online.

suppl_data

Please note: Oxford University Press is not responsible for the content or functionality of any supporting materials supplied by the authors. Any queries (other than missing material) should be directed to the corresponding author for the article.

APPENDIX A: EXTRA TABLES AND FIGURES

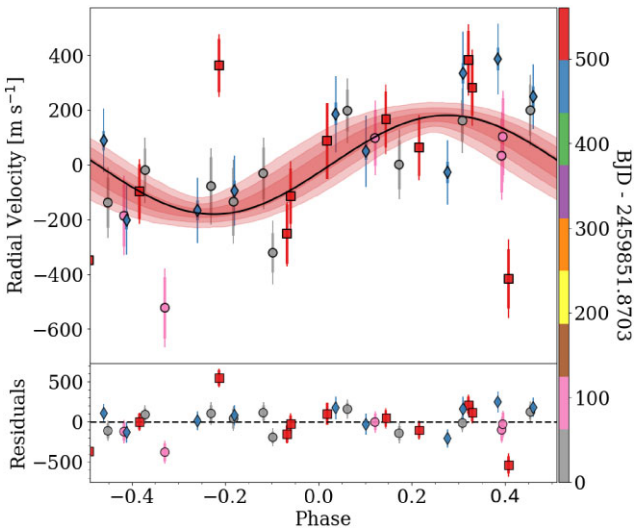

Figure A1. Top panel: RV phase-folded to the second Keplerian values associated to the stellar activity signal with fixed values from Table A2. Bottom panel: residuals to the best-fitting model.

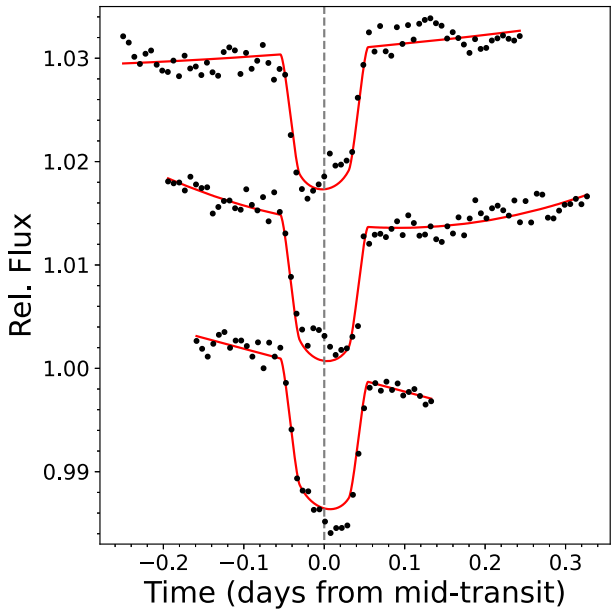

Figure A2. *TESS*-SPOC non-detrended time-series (in black) showing three potential spot-crossing events and stellar activity. A polynomial function was added to the transit model for visualization purposes (in red). QLP and CDIPS light curves were visually check, thus roughly showing the same spot-crossing patterns. Time flows from the top to bottom panels, with the first two events from Sector 33, while the transit at the bottom being from Sector 34.

Table A1. NGTS-33 ARIADNE priors.

Parameters	Prior	Hyperparameters
$T_{\rm eff}$	Normal	(7434,100^2)
log g	Normal	(4.3, 0.4^2)
[Fe/H]	Normal	(–0.13, 0.23^2)
Distance	Normal	(438,10^2)
R_s	Normal	(1.48, 0.5^2)
$A_{\rm V}$	Uniform	(0.00, 1.02)

Table A2. Properties for the second Keplerian.

Property	Value
P (d)	1.391 558 (fixed)
K ($\rm m\,s^{-1}$)	176±54
e	0.0 (fixed)
$\omega(^\circ)$	90 (fixed)
$\rm M_o(^\circ)$	64 (fixed)

A1 ARIADNE priors for the stellar characterization

A2 Global modelling: activity signal

A3 Transit-timing variation data

A4 Spot-crossing events on NGTS-33 and periodicity analysis on nearby object UCAC4 271–014742

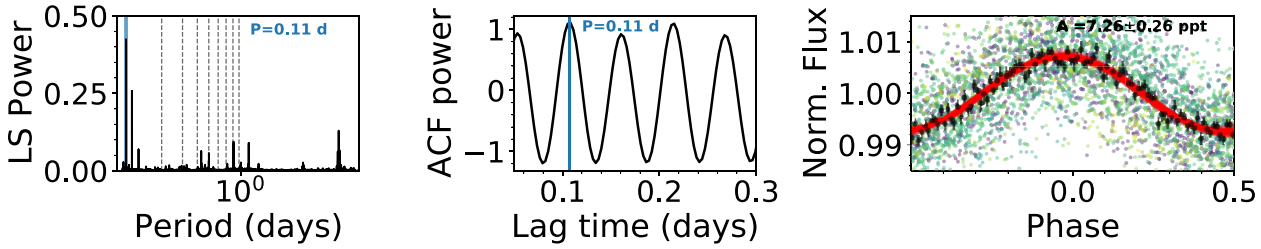

Figure A3. Rotation analysis on UCAC4 271-014742, a known pulsating variable star of $V = 13.9$ mag, period of 0.097 174 d from *GAIA*, and 32 arcsec away from NGTS-33. See Fig. 5 for comparison and Sections 3.3 and 3.1 for more information.

Table A3. NGTS-33 TTV data.

Time (d; BJD_{TDB})	OC (min)	Low error	Upper error	Pipeline
2458493.239828	1.153 99	1.54222	1.45155	*TESS*-SPOC
2458496.067799	–1.014 92	1.92430	1.91326	*TESS*-SPOC
2458498.895770	–1.829 14	1.89144	2.20077	*TESS*-SPOC
2458501.723741	–0.340 39	1.57699	1.59344	*TESS*-SPOC
2458504.551712	2.085 56	2.49663	2.06386	*TESS*-SPOC
2458507.379683	–1.101 07	1.74482	2.02213	*TESS*-SPOC
2458513.035625	-0.602 21	1.51767	1.54191	*TESS*-SPOC
2458515.863596	1.612 95	1.56667	1.47080	*TESS*-SPOC
2459225.684317	0.406 65	1.20163	1.24230	*TESS*-SPOC
2459228.512288	0.682 59	1.23309	1.13504	*TESS*-SPOC
2459231.340259	–1.487 32	1.21970	1.25541	*TESS*-SPOC
2459234.168230	-0.433 65	1.24079	1.25539	*TESS*-SPOC
2459236.996201	0.572 53	1.31606	1.35225	*TESS*-SPOC
2459239.824172	0.691 38	1.20454	1.23394	*TESS*-SPOC
2459242.652143	0.185 17	1.17847	1.20931	*TESS*-SPOC
2459245.480114	–0.404 57	1.36060	1.30785	*TESS*-SPOC
2459248.308085	–1.174 81	1.181 39	1.158 36	*TESS*-SPOC
2459253.964027	0.787 40	1.183 90	1.184 85	*TESS*-SPOC
2459256.791998	0.262 38	1.218 33	1.270 35	*TESS*-SPOC
2459259.619969	–0.976 29	1.180 17	1.191 00	*TESS*-SPOC
2459262.447940	0.121 03	1.187 87	1.192 00	*TESS*-SPOC
2459268.103882	–0.574 45	1.21199	1.242 92	*TESS*-SPOC
2459270.931853	–0.511 48	1.181 99	1.207 94	*TESS*-SPOC
2459273.759824	0.111 63	1.215 30	1.173 89	*TESS*-SPOC
2459276.587795	0.781 47	1.268 31	1.248 36	*TESS*-SPOC
2459963.784748	0.521 37	1.143 55	1.132 39	QLP
2459966.612719	–1.543 66	1.247 78	1.242 12	QLP
2459969.440690	0.106 03	1.093 43	1.045 11	QLP
2459972.268661	0.938 27	1.323 15	1.326 52	QLP
2459977.924603	1.111 41	1.450 05	1.392 17	QLP
2459980.752574	–0.13346	1.046 37	1.075 95	QLP
2459983.580545	–0.809 81	0.971 73	0.976 77	QLP
2459986.408516	0.511 74	1.006 39	1.017 24	QLP
2458846.736203	0.843 355	1.267 368	1.241 354	NGTS
2458880.671855	–0.571 765	1.229 419	1.120 578	NGTS
2458897.639681	–0.649 302	1.378 999	1.412 332	NGTS
2458914.607507	0.060 029	1.175 076	1.212 128	NGTS
2459174.780839	–0.262 582	1.045 301	1.142 524	NGTS
2459208.716491	0.745 968	1.103 477	1.067 075	NGTS
2459225.684317	–0.402 598	1.236 785	1.264 854	NGTS

This paper has been typeset from a TEX/LATEX file prepared by the author.